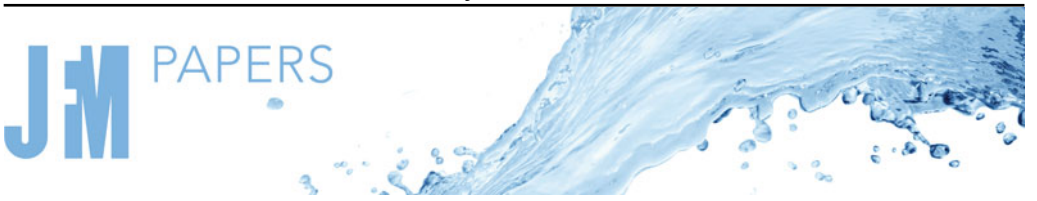
J. Fluid Mech. (2026), *vol.* 1037, A54, doi:10.1017/jfm.2026.11694



Wavemaker and endogeneity of gravitationally stretched weakly viscoelastic jets

Daniel Moreno-Boza

Grupo de Mecánica de Fluidos, Departamento de Ingeniería Térmica y Fluidos, Universidad Carlos III de Madrid, Spain

Corresponding author: Daniel Moreno-Boza, damoreno@ing.uc3m.es

(Received 24 February 2026 UTC; revised 15 April 2026 UTC; accepted 17 May 2026 UTC)

Highly stretched capillary jets produced by gravity are central to drop generation, micro-thread formation and extensional-rheometry concepts. For Newtonian fluids, the transition from steady jetting to self-excited oscillations in a gravitationally stretched jet is predicted accurately by one-dimensional slender-jet equations that retain the exact interfacial curvature and admit a global eigenvalue analysis (Rubio-Rubio *et al.* 2013, *J. Fluid Mech.*, vol. 729, pp. 471–483). Separately, weakly viscoelastic jets governed by Oldroyd-B/Giesekus constitutive laws exhibit elastocapillary regimes and beads-on-a-string dynamics that are well captured by one-dimensional free-surface models (Ardekani *et al.* 2010 *J. Fluid Mech.*, vol. 665, pp. 46–56). Here, we study the global linear stability of a one-dimensional full-curvature model for gravitationally stretched viscoelastic jets in the Oldroyd-B limit. We first benchmark the Newtonian limit, reproducing marginal spectra and base-flow profiles, and then quantify how elasticity shifts the critical jetting–dripping boundary by tracking the leading global Hopf eigenpair across the rheological parametric space. For experimentally relevant moderate elasticity, characterised by order-unity Deborah numbers, polymeric tension modifies both the critical Weber number and the selected oscillation frequency, and endogeneity, i.e. the local contribution of the unperturbed flow dynamics to the selected global eigenvalue, reveals that marginality results from a balance between capillary/kinematic contributions and an additional elastic-stress feedback pathway. To interpret and predict the onset mechanism, we compute wavemakers and receptivity/structural-sensitivity fields from direct–adjoint eigenfunctions, showing that viscoelasticity broadens the sensitivity region downstream while the adjoint remains strongly localised near the inlet, thereby identifying the near-nozzle region as the dominant receptive location.

Key words: capillary flows, viscoelasticity, instability

© The Author(s), 2026. Published by Cambridge University Press. This is an Open Access article, distributed under the terms of the Creative Commons Attribution licence (https://creativecommons.org/licenses/by/4.0/), which permits unrestricted re-use, distribution and reproduction, provided the original article is properly cited.

https://doi.org/10.1017/jfm.2026.11694 Published online by Cambridge University Press

1. Introduction and motivation

The controlled generation of micron- and sub-micron-sized threads, films and droplets is central to a wide range of technologies in medicine, pharmaceutics, chemical engineering and materials science (e.g. Basaran 2002; Stone, Stroock & Ajdari 2004; Barrero & Loscertales 2007; Utada *et al.* 2007; Eggers & Villermaux 2008). A recurring strategy is to produce a liquid filament whose diameter is substantially smaller than that of the injector, thereby avoiding the fabrication and operation of micro-scale solid geometries. This idea underpins classical fibre-spinning configurations (Pearson & Matovich 1969; Denn 1980), electrospinning devices where electrical stresses stretch the jet (Doshi & Reneker 1995; Loscertales *et al.* 2002; Marín *et al.* 2007) and flow-focusing/co-flow arrangements that generate thin inner jets and micro-drops through capillary breakup (Gañán-Calvo 1998; Gañán-Calvo & Gordillo 2001; Anna, Bontoux & Stone 2003; Suryo & Basaran 2006; Utada *et al.* 2007; Marín *et al.* 2009; Castro-Hernández *et al.* 2012). In this landscape, gravitational stretching provides a particularly robust and conceptually simple route: a millimetric nozzle can generate a long, slender thread that thins downstream under the combined action of gravity and continuity, producing droplets or micro-threads whose characteristic scale can be far smaller than the injector size (Eggers & Villermaux 2008; Rubio-Rubio, Sevilla & Gordillo 2013).

For Newtonian liquids injected vertically downwards, the dynamics exhibits a sharp transition between a steady jetting regime and a dripping regime in which drops detach directly from the nozzle. A long filament develops only when the imposed flow rate exceeds a critical threshold $Q_c(\rho, \nu, \sigma, g, R)$ (or, in non-dimensional form, a critical Weber number), which depends on density ρ, kinematic viscosity ν, surface tension σ, gravity g and nozzle radius R (Rubio-Rubio *et al.* 2013). Experiments also show a hysteretic behaviour, for which the critical flow rate for the disappearance of an initially long jet (jetting to dripping) is lower than that required to form a long jet when increasing the flow rate starting from dripping (Clanet & Lasheras 1999; Ambravaneswaran *et al.* 2004). Since the minimum achievable drop size for a given liquid and injector decreases with the critical flow rate, the jetting-to-dripping boundary is the relevant stability limit when the objective is to sustain the thinnest possible steady threads while minimising injector complexity (Rubio-Rubio *et al.* 2013).

From a theoretical viewpoint, early attempts to rationalise the jetting–dripping transition invoked local (parallel-flow) spatio-temporal stability analyses of capillary jets. For a uniform cylindrical jet, Leib & Goldstein (1986) showed that there exists a critical flow rate below which the flow becomes absolutely unstable and a spatial analysis is not well posed (see also Keller, Rubinow & Tu 1973); in this framework the transition is often discussed in terms of convective versus absolute amplification. A useful point of contact with the present study is the local spatio-temporal analysis of Alhushaybari & Uddin (2019), who examine convective and absolute instability of a viscoelastic jet falling under gravity by deriving a dispersion relation for axisymmetric travelling-wave modes about a slowly varying slender base state and then applying standard pinch-point criteria in the complex wavenumber and frequency planes. The main strength of such local approaches is their diagnostic clarity: they provide a direct regime classification in terms of convective versus absolute instability and enable rapid parameter sweeps without solving a global eigenvalue problem. Their limitation in the strongly stretched regime is that the base flow is treated as quasi-parallel over the perturbation scale, whereas in gravitationally stretched jets the radius and velocity can vary on the same axial scale as the instability core and the nozzle boundary conditions play a decisive role in selecting the observed global oscillator. In that case, a global formulation retains the non-parallel base state and

https://doi.org/10.1017/jfm.2026.11694 Published online by Cambridge University Press

boundary conditions and yields discrete global eigenpairs with onset frequencies, together with structural-sensitivity diagnostics that quantify where and through which couplings the instability is selected. This perspective explains why local wave-train predictions can become, at best, order-of-magnitude estimates of the experimentally observed thresholds in gravitationally stretched jets (Rubio-Rubio *et al.* 2013), and it motivates the use of global-stability analyses when quantitative marginal curves and receptivity mechanisms are sought. In the present viscoelastic setting, the point is therefore not only that the base state is non-parallel, but also that the quantities of interest are intrinsically global, namely, the selected discrete Hopf mode and its associated direct–adjoint receptivity structure cannot be inferred from a local dispersion relation alone, even when the latter remains useful for diagnosing convective/absolute tendencies.

Several studies have therefore incorporated non-parallel and global effects in the dripping–jetting problem. Schulkes (1994) obtained a dripping–jetting transition in the ideal-flow limit; for inertia-dominated jets, Le Dizès (1997) identified a global mechanism preventing the formation of a slender jet at low exit velocities and Senchenko & Bohr (2004) used multiple-scale methods to quantify a stabilising influence of gravity on capillary perturbations. In addition, viscous relaxation of the exit velocity profile can play an important role in low-viscosity liquids and long injectors, improving agreement between theory and experiments when incorporated appropriately (Sevilla 2011). In the gravitationally stretched regime of interest here, a key step was taken by Sauter & Buggisch (2005), who combined experiments and a global linear analysis for very viscous jets and identified the self-excited global mode associated with the onset of unsteadiness. Later, Rubio-Rubio *et al.* (2013) demonstrated that one-dimensional slender-jet equations can predict not only the critical flow rate but also the oscillation frequency at onset over wide ranges of viscosity and nozzle diameter, provided that the exact interfacial curvature is retained (see also Eggers & Dupont 1994; García & Castellanos 1994). A central conclusion of that work is that axial curvature, which is already recognised as stabilising in the classical Plateau–Rayleigh setting, plays an essential stabilising role in strongly stretched jets, especially for large Bond numbers, thereby reshaping the stability boundary in practically relevant non-slender configurations (Rubio-Rubio *et al.* 2013).

More recently, and in the vein of non-parallel effects, Sun *et al.* (2026) examined the dripping–jetting transition for capillary jets issuing with a relaxing nozzle-exit velocity profile by combining experiments and global-stability analysis. They showed that velocity relaxation systematically lowers the critical Weber number and that this effect cannot be captured reliably by classic local spatio-temporal theory, since the upstream relaxation region generates strongly non-parallel global disturbances with enhanced radial–axial coupling, especially at sufficiently large Reynolds number. Their results further underline the importance of global formulations when the spatial development of the basic flow and disturbance field are both essential to the transition mechanism.

Parallel to these developments, polymer solutions and other weakly elastic liquids are known to exhibit a markedly different thinning and breakup dynamics relative to Newtonian liquids. Even at dilute concentrations, extensional stresses can delay pinch-off, promote elastocapillary thinning and generate beads-on-a-string morphologies; these regimes have been captured quantitatively with one-dimensional free-surface models coupled to Oldroyd-B or Giesekus constitutive laws, enabling inference of the extensional rheology from the evolution of jets and filaments (Ardekani, Sharma & McKinley 2010). Moreover, dispensing and jetting experiments in polymer solutions reveal additional dynamical regimes and transitions, including oscillatory behaviours, that depend sensitively on elasticity and on the interplay between gravity, capillarity and extensional stress (Clasen *et al.* 2009). Complementing these experimental observations,

https://doi.org/10.1017/jfm.2026.11694 Published online by Cambridge University Press

local spatio-temporal analyses of viscoelastic jets under gravity have also quantified how elasticity can shift convective and absolute instability boundaries and thereby modify the conditions for unsteadiness (Alhushaybari & Uddin 2019), as pointed out above. Together, these results suggest that the critical flow rate and the onset mechanism in gravitationally stretched jets should be substantially modified by viscoelasticity in experimentally accessible parameter ranges.

A key open direction, therefore, is to determine how weak viscoelasticity modifies global-mode selection, receptivity and eigenvalue production in jets that are simultaneously (i) strongly stretched by gravity and (ii) governed by a viscoelastic constitutive dynamics. Beyond determining how the marginal conditions, defined by a critical flow rate, and the associated onset frequency shift with the corresponding rheological parameters, two complementary direct–adjoint analyses are especially useful in the present problem. First, the wavemaker, or structural sensitivity, identifies the region where the global mode is most sensitive to a localised feedback perturbation of the linear dynamics (Giannetti & Luchini 2007). In physical terms, it marks the part of the jet where a small local change in the coupling between variables would produce the largest shift in the selected global mode, and may therefore be regarded as the core of the global feedback loop. Second, the endogeneity analysis quantifies how much each axial location contributes, through the unperturbed local dynamics itself, to the global growth rate and oscillation frequency (Marquet & Lesshafft 2015). It therefore provides a local budget of eigenvalue production, distinguishing where the instability is most sensitive from where the mode is actually being selected. In the present setting these diagnostics are particularly appealing, since gravitational stretching produces a spatially developing base state whose instability core may remain localised near the inlet while the observable dynamics extends far downstream. The wavemaker then isolates the effective feedback region, whereas the endogeneity reveals how capillary, inertial and viscoelastic effects combine spatially to determine the selected eigenvalue.

More recent work has broadened the Newtonian jetting picture by explicitly targeting mechanisms that sit beyond the onset eigenvalue itself, including geometric confinement, noise-driven amplification and forced receptivity. In particular, Martínez-Calvo *et al.* (2018) extended the global framework of Sauter & Buggisch (2005) and Rubio-Rubio *et al.* (2013) to axially confined jets whose lower end interacts with a bath, and showed that the confinement length L is an additional control parameter that shifts the critical flow rate and can even introduce an intermediate nonlinear regime of sustained limit-cycle oscillations without breakup, denoted oscillatory jetting. In the globally stable jetting regime, Le Dizès & Villermaux (2017) instead focused on how perturbations grow convectively and quantified optimal spatial gains using a Wentzel-Kramers-Brillouin-Jeffreys approach for both nozzle forcing and distributed background noise, thereby linking breakup length, dominant wavelength and droplet size to a noise-amplification mechanism rather than to a discrete unstable global mode. These questions naturally connect to non-modal viewpoints, and Shukla & Gallaire (2020) pursued this direction by combining nonlinear simulations with a global resolvent analysis of gravitationally stretched jets in the stable regime, extracting the optimal forcing frequency and spatial response while highlighting a pronounced dependence on forcing amplitude when gravity-induced non-parallelism is active. For a broader review of tip-streaming and jetting configurations, including global-stability analysis, short-term response/non-normal effects and oscillatory jetting in related axisymmetric free-surface flows, see Montanero (2024). Finally, Sun *et al.* (2024) incorporated insoluble surfactants and Marangoni stresses into a global model and carried out both global stability and global resolvent analyses, showing that surfactants and gravity stabilise the base state while gravitational stretching can shift the optimal

https://doi.org/10.1017/jfm.2026.11694 Published online by Cambridge University Press

forcing frequency away from the intrinsic one for stable jets, whereas near criticality a resonance-like response locks the optimal forcing to the leading global frequency. Collectively, these studies emphasise that, in stretched jets, the observed unsteadiness can reflect a competition between intrinsic global modes and strong convective or forced amplification shaped by non-parallelism, boundary conditions and additional interfacial physics, which motivates treating frequency selection, receptivity and sensitivity within a global framework.

The paper is structured as follows: § 2 formulates the one-dimensional slender-jet model for gravitationally stretched viscoelastic jets, § 3 derives the linearised equations about the steady base state and summarises the global eigenvalue formulation, the discrete adjoint problem and the wavemaker/endogeneity diagnostics used to interpret the instability mechanism. Section 4 presents selected case studies, § 5 uses wavemaker and endogeneity decompositions to identify the regions and couplings responsible for eigenvalue selection and § 6 quantifies how viscoelasticity shifts marginal conditions and onset frequencies. We conclude in § 7 with a brief discussion of implications and open directions.

2. Mathematical description

We consider an incompressible axisymmetric slender viscoelastic jet with radius $r(z,t)$ and mean axial velocity $u(z,t)$. The solvent has constant density ρ and viscosity μ_s, whereas the polymer is characterised by its viscosity μ_p and relaxation time λ. The liquid–air surface tension coefficient is σ, assumed constant as well. The description of the jet dynamics combines the leading-order mass and momentum equations, derived originally by Eggers & Dupont (1994), augmented by the extra stresses due to the presence of the polymer (Ardekani *et al.* 2010), given by

$$\partial_t\left(r^2\right)+\partial_z\left(ur^2\right)=0, \tag{2.1}$$

and

$$\rho\left(\partial_t u+u\,\partial_z u\right)=\rho g-\sigma\,\partial_z\mathcal{C}+\frac{3\mu_s}{r^2}\partial_z\left(r^2\,\partial_z u\right)+\frac{1}{r^2}\partial_z\left(r^2\,T\right), \tag{2.2}$$

where g is the gravitational acceleration, $\mathcal{C}$ is the full curvature,

$$\mathcal{C}=\frac{1}{r}\left(1+r_z^2\right)^{-1/2}-r_{zz}\left(1+r_z^2\right)^{-3/2}, \tag{2.3}$$

and $T=\tau_{zz}-\tau_{rr}$ is the polymeric tensile stress, written in terms of the diagonal components of the polymeric extra-stress tensor $\boldsymbol{\tau}$. The evolution of $\boldsymbol{\tau}$ is assumed to be dictated by the Oldroyd-B/Giesekus constitutive model

$$\boldsymbol{\tau}+\lambda\overset{\triangledown}{\boldsymbol{\tau}}+\frac{\alpha\lambda}{\mu_p}\,\boldsymbol{\tau}\cdot\boldsymbol{\tau}=2\mu_p\,\boldsymbol{D}, \tag{2.4}$$

with $\boldsymbol{D}=1/2(\nabla\boldsymbol{v}+\nabla\boldsymbol{v}^T)$, $\overset{\triangledown}{\boldsymbol{\tau}}=\mathrm{D}/\mathrm{D}t\,\boldsymbol{\tau}-(\nabla\boldsymbol{v})^T\cdot\boldsymbol{\tau}-\boldsymbol{\tau}\cdot(\nabla\boldsymbol{v})$ the upper-convected derivative, $(\mathrm{D}/\mathrm{D}t)$ the material derivative operator and α is the Giesekus mobility factor. Note that setting $\alpha=0$ recovers the Oldroyd-B model, which will be the choice for the rest of this paper. The diagonal components of (2.4) read

$$\lambda\left(\partial_t\tau_{zz}+u\partial_z\tau_{zz}-2\,u_z\,\tau_{zz}\right)+\tau_{zz}+\frac{\alpha\lambda}{\mu_p}\,\tau_{zz}^2=2\mu_p\,u_z, \tag{2.5}$$

$$\lambda\left(\partial_t\tau_{rr}+u\,\partial_z\tau_{rr}+u_z\,\tau_{rr}\right)+\tau_{rr}+\frac{\alpha\lambda}{\mu_p}\,\tau_{rr}^2=-\mu_p\,u_z. \tag{2.6}$$

https://doi.org/10.1017/jfm.2026.11694 Published online by Cambridge University Press

Note that, whereas finite extensible nonlinear elastic models are more appropriate when the polymer approaches its finite extension limit, since the present study concerns the weakly elastic, early linear stage of the instability about a steady stretched base state, the Giesekus/Oldroyd-B closure is deemed as a baseline constitutive model, while finite extensibility is more appropriate in scenarios with stronger stretching and/or nonlinear post-critical dynamics.

The mathematical description is completed upon boundary conditions, namely,

$$r(0,t) - R = u(0,t) - \frac{Q}{\pi R^2} = \tau_{zz}(0,t) = \tau_{rr}(0,t) = 0, \tag{2.7}$$

where R is the nozzle radius and Q is the prescribed flow rate. The assumption of fully relaxed polymer at the exit, $\tau_{zz}(0) = \tau_{rr}(0) = 0$, provides a minimal and internally consistent closure for a free-jet model posed only for $z \geqslant 0$. It is appropriate when the residence time in the injector is long compared with the relaxation time λ and when upstream deformation rates are weak. At the same time, it is not expected to be universally accurate in experiments, since polymer solutions may exit the injector with a non-negligible elastic memory of the internal shear and extension history, as evidenced by the classical die-swell (Barus) effect. In particular, extrudate swell in dilute polymer solutions is driven primarily by shear-generated normal stresses, notably the first normal-stress difference, rather than by a stress-free state at the die exit (e.g. Mitsoulis 2010), and elasticity is known to influence jetting–dripping thresholds in related jetting configurations (Montanero & Gañán-Calvo 2008).

In the present work we nevertheless adopt (2.7) as the reference inlet-stress condition. The reason is that any non-zero specification of $\tau_{zz}(0)$ and $\tau_{rr}(0)$ within a reduced free-surface jet model remains an effective closure unless the internal nozzle flow and die-exit region are modelled explicitly. Asymptotic inlet-stress relations derived from the outer jet equations, as in local slender analyses of viscoelastic jets under gravity (Alhushaybari & Uddin 2019), provide mathematically consistent alternatives, but they still do not encode the dependence on injector geometry, entrance effects or residence-time history that controls die swell in practice. Likewise, prescribing finite inlet stresses directly introduces additional closure parameters whose values are not fixed by the present reduced model alone. For these reasons, the relaxed condition (2.7) should be interpreted here as a baseline choice that isolates the role of viscoelasticity in the downstream stretched-jet dynamics, rather than as a universally realistic experimental boundary condition. To assess the robustness of the main conclusions, we examine in Appendix C the sensitivity of the base state and global-stability metrics to be defined below to alternative non-zero inlet-stress closures. A fully coupled nozzle–jet description, or a calibrated inlet condition based on independent measurements of die swell and upstream rheology, remains a natural extension of the present framework and is left for future work.

Lastly, initial conditions are also needed for the temporal marching of the model. We shall describe them below if needed.

2.1. *Choice of scales and non-dimensionalisation*

Following Rubio-Rubio *et al.* (2013), we take the gravito–capillary scales

$$\ell_\sigma = \left(\frac{\sigma}{\rho g}\right)^{1/2}, \quad U_\sigma = \sqrt{g\ell_\sigma}, \quad T_\sigma = \sqrt{\ell_\sigma / g}, \quad \tau_c = \mu_p U_\sigma / \ell_\sigma, \tag{2.8}$$

as relevant scales for length, velocity, time and polymer stress, respectively. With these choices, the dimensionless model reads

$$\partial_t\left(r^2\right) + \partial_z\left(ur^2\right) = 0, \tag{2.9}$$

https://doi.org/10.1017/jfm.2026.11694 Published online by Cambridge University Press

$$\partial_t u + u\,\partial_z u = 1 - \partial_z \mathcal{C} + \frac{\Gamma}{r^2}\partial_z\Big(r^2\,\partial_z u\Big) + \frac{\Gamma(1-\beta)}{3\beta r^2}\partial_z\big(r^2\,T\big), \tag{2.10}$$

$$De\big(\partial_t \tau_{zz} + u\,\partial_z \tau_{zz} - 2\,u_z\,\tau_{zz}\big) + \tau_{zz} + \alpha De\,\tau_{zz}^2 = 2u_z, \tag{2.11}$$

$$De\big(\partial_t \tau_{rr} + u\,\partial_z \tau_{rr} + u_z\,\tau_{rr}\big) + \tau_{rr} + \alpha De\,\tau_{rr}^2 = -\,u_z, \tag{2.12}$$

where each dependent variable should be understood as scaled with (2.8), i.e. $z \to z/\ell_\sigma$, $u \to u/U_\sigma$, $t \to t/T_\sigma$, $\tau_{ij} \to \tau_{ij}/\tau_c$. In these units, the dimensionless counterpart of the baseline boundary conditions (2.7) is given by

$$r(0,t) = Bo^{1/2}, \quad u(0,t) = We^{1/2}Bo^{-1/4}, \quad \tau_{zz}(0,t) = \tau_{rr}(0,t) = 0. \tag{2.13}$$

Alternative non-zero inlet-stress closures are examined separately in Appendix C. Suitable outlet conditions must also be prescribed downstream in order to numerically integrate these equations. A possible choice is a jet with zero axial curvature, i.e. $r_z = r_{zz} = 0$, at $z = L \gg 1$, as done for instance by Shukla & Gallaire (2020). Above, $Bo = \rho g R^2/\sigma$ is the Bond number, $We = \rho U^2 R/\sigma$ is the Weber number based on the mean exit speed $U = Q/(\pi R^2)$, $\Gamma = 3\nu_s/\sqrt{g\ell_\sigma^3}$ is the Kapitza number based on the solvent kinematic viscosity $\nu_s = \mu_s/\rho$, $De = \lambda/T_\sigma = \lambda\sqrt{g/\ell_\sigma}$ is the Deborah number and $\beta = \mu_s/(\mu_s + \mu_p)$ is the solvent-to-total viscosity ratio. Finally, note that the Newtonian limit is recovered for $1 - \beta = De = 0$. It is worth noting that the stress scale $\tau_c = \mu_p U_\sigma/\ell_\sigma$ measures the polymer stress relative to its own polymer-viscous scale, whereas its feedback on the momentum equation is weighted by the prefactor $(1-\beta)/\beta$. Thus, for $\beta \lesssim 1$ the dimensionless stress fields may remain $O(1)$ while their dynamical effect on the jet becomes asymptotically weak; in the exact limit $\beta = 1$, the polymer contribution vanishes and the appropriate description is the Newtonian system obtained by dropping the polymer-stress equations altogether.

2.2. *A note on rheological parameters*

In order to make sure that the rheological parameters, mostly De and β, remain within a realisable experimental range, we compute their values for a couple of examples from Clasen *et al.* (2012). In their 'map of misery' study they prepare (i) a polystyrene solution (PS) in diethyl phthalate (DEP) and (ii) a polyisobutylene solution (PIB) in pristane (an isoparaffinic hydrocarbon), and report the corresponding material properties (ρ, σ, λ). Using scales (2.8), these two canonical polymer solutions map to $De \simeq 1.68$ (PS in DEP: $\rho = 1118\ \mathrm{kg\,m^{-3}}$, $\sigma = 37.5\ \mathrm{mN\,m^{-1}}$, $\lambda = 0.023$ s) and $De \simeq 4.22$ (PIB in pristane: $\rho = 793.7\ \mathrm{kg\,m^{-3}}$, $\sigma = 24.9\ \mathrm{mN\,m^{-1}}$, $\lambda = 0.057$ s), directly justifying a focus on moderate elasticity $De = O(1)$. Finally, their third viscoelastic reference liquid is a Boger fluid, namely a (nearly) constant-shear-viscosity elastic liquid obtained by dissolving a trace amount of high-molecular-weight PIB in a high-viscosity, low-molecular-weight PIB matrix; this illustrates in practice how elasticity can be tuned largely independently of the shear-viscosity level. In our notation, this corresponds to the experimentally accessible regime where the 'solvent-like' contribution dominates the shear viscosity (i.e. β closer to 1), while the polymeric relaxation time (and thus De) can be made very large if desired.

3. The linearised equations

We assume the usual normal-mode decomposition for each fluid variable $\boldsymbol{q} = [r, u, \tau_{zz}, \tau_{rr}]^{\mathrm{T}}$ about a steady base

$$\boldsymbol{q}(z,t) = \boldsymbol{q}_0(z) + \epsilon\hat{\boldsymbol{q}}(z)\mathrm{e}^{\omega t}, \tag{3.1}$$

https://doi.org/10.1017/jfm.2026.11694 Published online by Cambridge University Press

where $\epsilon \ll 1$ is an arbitrarily small number, $\boldsymbol{q}_0(z)$ is the steady solution to (2.10)–(2.12), $\omega = \omega_r + \mathrm{i}\omega_i$ is a complex growth rate whose real and imaginary parts represent the temporal amplification rate and oscillation frequency, respectively, and $\hat{\boldsymbol{q}}$ are (direct) eigenfunctions. Substituting the ansatz (3.1) into (2.10)–(2.12) and collecting $O(\epsilon)$ terms yields a linear system that can be written in compact form as the generalised eigenvalue problem

$$(\mathcal{A} - \omega\mathcal{B})\,\hat{\boldsymbol{q}} = \boldsymbol{0}, \tag{3.2}$$

where $\mathcal{A}$ and $\mathcal{B}$ are linear differential operators encompassing boundary conditions. We employ a standard Chebyshev collocation technique in order to discretise (3.2) (see Appendix B for details) which in turn yields the matrix pencil $(\boldsymbol{A} - \omega\boldsymbol{B})\tilde{\boldsymbol{q}} = 0$, where $\boldsymbol{A}$, $\boldsymbol{B}$ and $\tilde{\boldsymbol{q}}$ represent the discretised counterparts, whose spectrum ω determines the global temporal stability of the spatially varying base flow. This full-curvature formulation recovers the Newtonian stretched-jet framework of Rubio-Rubio *et al.* (2013) in the appropriate limit and here serves as the basis for a direct–adjoint analysis of weakly viscoelastic mode selection. Because the base state varies significantly with z under gravitational acceleration and capillary thinning, local parallel stability theory is insufficient to capture the onset of self-excited jet oscillations. Thus, a global approach is the correct strategy to predict stability thresholds and oscillation frequencies in the jetting regime. In the discretised setting, we define a weighted inner product consistent with the spectral collocation quadrature

$$\langle \boldsymbol{a}, \boldsymbol{b} \rangle_{\boldsymbol{Q}} \equiv \boldsymbol{a}^{\mathrm{H}}\,\boldsymbol{Q}\,\boldsymbol{b}, \tag{3.3}$$

where $(\cdot)^{\mathrm{H}}$ denotes the conjugate transpose and $\boldsymbol{Q}$ is a Hermitian positive–definite weight matrix assembled from the collocation weights (see, for instance, Trefethen (2000)). Direct eigenfunctions are normalised such that

$$\langle \tilde{\boldsymbol{q}}, \tilde{\boldsymbol{q}} \rangle_{\boldsymbol{Q}} = 1. \tag{3.4}$$

To quantify the sensitivity of the global modes to localised modifications of the base flow and/or of the linear operator, we also introduce the corresponding adjoint (left) eigenfunctions. From a mathematical standpoint, the adjoint eigenfunction provides the receptivity kernel of the global oscillator, i.e. it weights external forcing and initial perturbations in the energy inner product, thereby filtering generic disturbances into the component that most efficiently excites the selected direct mode and pinpointing the region(s) of strongest feedback sensitivity. The (discrete) adjoint eigenfunctions $\tilde{\boldsymbol{q}}^{\dagger}$ are then defined as solutions of the Q-adjoint generalised eigenvalue problem

$$\left(\boldsymbol{A}^{\dagger} - \bar{\omega}\,\boldsymbol{B}^{\dagger}\right)\tilde{\boldsymbol{q}}^{\dagger} = \boldsymbol{0}, \quad \boldsymbol{A}^{\dagger} = \boldsymbol{Q}^{-1}\boldsymbol{A}^{\mathrm{H}}\boldsymbol{Q}, \quad \boldsymbol{B}^{\dagger} = \boldsymbol{Q}^{-1}\boldsymbol{B}^{\mathrm{H}}\boldsymbol{Q}, \tag{3.5}$$

and we impose the standard bi-orthogonality (normalisation) condition

$$\left\langle \tilde{\boldsymbol{q}}^{\dagger}, \boldsymbol{B}\,\tilde{\boldsymbol{q}} \right\rangle_{\boldsymbol{Q}} = \tilde{\boldsymbol{q}}^{\dagger\mathrm{H}}\boldsymbol{Q}\,\boldsymbol{B}\,\tilde{\boldsymbol{q}} = 1, \tag{3.6}$$

which enables a direct projection of perturbations onto individual global modes.

Building on this framework, we characterise the spatial structure of the global instability using two complementary analyses based on the sensitivity of eigenvalues with respect to localised changes of the operator $\mathcal{A}$. First, the wavemaker (or structural sensitivity) field measures the sensitivity of ω to a localised feedback perturbation of the operator and is typically constructed from the pointwise overlap of the direct and adjoint eigenfunctions; it highlights the region where the instability mechanism is most receptive to modifications

https://doi.org/10.1017/jfm.2026.11694 Published online by Cambridge University Press

of the local coupling between state variables, and is therefore a proxy for the core of the global feedback loop (Giannetti & Luchini 2007). Equivalently, the wavemaker identifies the spatial region where cause and effect overlap most strongly. The direct mode is large enough there for the local dynamics to matter, and the adjoint mode is also large enough there for the eigenvalue to react strongly to a perturbation. For that reason, it is often interpreted as the core of the global oscillator, namely the part of the flow where a small structural change has the greatest impact on the selected growth rate and frequency. It is defined as the real scalar

$$S(z) = \left\| \boldsymbol{Q}\tilde{\boldsymbol{q}}^{\dagger} \right\| \, \|\tilde{\boldsymbol{q}}\| \,, \tag{3.7}$$

which corresponds to the Frobenius norm of the structural-sensitivity tensor

$$\boldsymbol{S} = \boldsymbol{Q}\tilde{\boldsymbol{q}}^{\dagger} \otimes \tilde{\boldsymbol{q}}. \tag{3.8}$$

Additionally, the momentum-restricted wavemaker is defined as

$$S_{mom}(z) = \left\| \boldsymbol{U}\big(\boldsymbol{Q}\tilde{\boldsymbol{q}}^{\dagger}\big) \right\| \, \|\boldsymbol{U}\tilde{\boldsymbol{q}}\| \,, \tag{3.9}$$

where $\boldsymbol{U}$ is a projection matrix that extracts the subset of state components associated with the momentum equation. Numerically, the wavemaker is assembled node by node on the collocation grid. For each axial point z_j, one extracts the local direct and adjoint state vectors and computes the corresponding Euclidean norm in state space. Thus $S(z_j)$ is the Frobenius norm of the local structural-sensitivity tensor, whereas $S_{mom}(z_j)$ is the same quantity restricted to the momentum component through the projector $\boldsymbol{U}$. The reader is referred to Giannetti & Luchini (2007), Pralits, Brandt & Giannetti (2010) and Marquet & Lesshafft (2015) for implementation details.

Second, the endogeneity $E = E_r + \mathrm{i}E_i$, defined as

$$E(z) = \tilde{\boldsymbol{q}}^{\dagger} \cdot (\boldsymbol{A}\tilde{\boldsymbol{q}}), \tag{3.10}$$

where the dot indicates scalar multiplication of two vectors, provides a local budget for eigenvalue selection by quantifying the pointwise contribution of the unperturbed operator acting on the direct mode, weighted by the adjoint mode. In its discrete form, it yields a spatial density whose integral recovers the eigenvalue, namely,

$$\int_0^L E(z)\,\mathrm{d}z = \omega, \tag{3.11}$$

and whose real and imaginary parts can be interpreted as contributions to growth-rate and frequency selection, respectively (Marquet & Lesshafft 2015). Accordingly, $\mathrm{Re}(E)$ can be read as a local contribution to amplification or decay, while $\mathrm{Im}(E)$ gives the local contribution to frequency selection. In the present discrete implementation, the vector $\boldsymbol{A}\tilde{\boldsymbol{q}}$ is naturally partitioned into the four equation blocks associated with continuity, momentum and the two polymer-stress transport equations, thus one can write

$$\boldsymbol{A}\tilde{\boldsymbol{q}} = \begin{bmatrix} (\boldsymbol{A}\tilde{\boldsymbol{q}})_{cont} \\ (\boldsymbol{A}\tilde{\boldsymbol{q}})_{mom} \\ (\boldsymbol{A}\tilde{\boldsymbol{q}})_{\tau_{zz}} \\ (\boldsymbol{A}\tilde{\boldsymbol{q}})_{\tau_{rr}} \end{bmatrix}. \tag{3.12}$$

Accordingly, the total endogeneity is decomposed as

$$E(z) = E_{cont}(z) + E_{mom}(z) + E_{\tau_{zz}}(z) + E_{\tau_{rr}}(z), \tag{3.13}$$

https://doi.org/10.1017/jfm.2026.11694 Published online by Cambridge University Press

where

$$E_{cont} = \tilde{r}^{\dagger}(\boldsymbol{A}\tilde{\boldsymbol{q}})_{cont}, \quad E_{mom} = \tilde{u}^{\dagger}(\boldsymbol{A}\tilde{\boldsymbol{q}})_{mom}, \quad E_{\tau_{zz}} = \tilde{\tau}_{zz}^{\dagger}(\boldsymbol{A}\tilde{\boldsymbol{q}})_{\tau_{zz}}, \quad E_{\tau_{rr}} = \tilde{\tau}_{rr}^{\dagger}(\boldsymbol{A}\tilde{\boldsymbol{q}})_{\tau_{rr}}. \tag{3.14}$$

Together, wavemaker and endogeneity allow us to distinguish where the flow is most sensitive to localised perturbations (wavemaker) from where the eigenvalue is intrinsically produced by the dynamics of the unperturbed base state (endogeneity), thereby providing a sharp picture of the regions controlling global instability in stretched Newtonian and viscoelastic jets. In the present context, this distinction is especially useful because the region where the jet is most receptive need not coincide exactly with the region where the capillary, inertial and viscoelastic contributions combine to select the eigenvalue.

4. Selected case studies

This section presents a set of representative case studies designed to (i) benchmark the present base-flow and global-stability formulation against established Newtonian results and (ii) illustrate, in a systematic manner, how weak elasticity modifies both the onset and the structure of the global oscillatory instability. We focus on parameter combinations that lie close to marginality so that (a) the leading eigenpair is cleanly separated from the rest of the spectrum and (b) small changes in rheology produce measurable eigenvalue drift. The first case reproduces the nearly marginal Newtonian jetting configuration of Rubio-Rubio *et al.* (2013) and serves as a reference for our numerical implementation (base state, spectrum and eigenfunctions), after which we introduce viscoelasticity at fixed viscosity ratio to quantify the role of polymeric tension in the linear dynamics. The second case is a nearly marginal viscoelastic jet for which we validate the global-mode prediction by direct time marching of the nonlinear one-dimensional equations under a weak, transient inlet perturbation. Together, these two cases establish the reliability of the global framework and provide the building blocks for the mechanistic assessment developed below (wavemaker, endogeneity and their decomposition), as well as for the parametric trends in marginal conditions discussed subsequently.

4.1. *The case* $We = 3 \times 10^{-3}$, $Bo = 1.81$, $\Gamma = 5.83$

This case serves as a benchmark for our base-flow and linear-stability results. In the Newtonian limit, $1 - \beta = De = 0$, Rubio-Rubio *et al.* (2013) identified this parameter combination as nearly marginal, i.e. the leading global mode has vanishing growth rate, $\omega_r \simeq 0$, while oscillating at $\omega_i \simeq 0.325$, thereby fixing the critical flow rate (Weber number) for a prescribed liquid (Kapitza number) and nozzle diameter (Bond number) at the onset of self-sustained jet oscillations in the jetting–dripping transition. Figures 1(*a*) and 1(*c*) show that our global spectrum and base-state radius $r_0(z)$ accurately reproduce the reference Newtonian results, including the marginal leading complex-conjugate pair and the weakly non-parallel thinning of the jet. We then extend this benchmark by introducing viscoelasticity at fixed solvent-to-total viscosity ratio $\beta = 0.5$, considering $De = 3$ and $De = 5$. The spectrum in figure 1(*a*) shows that order-unity (and larger) Deborah numbers are required for the leading eigenvalue to drift appreciably, meaning that increasing De shifts the dominant pair towards more negative ω_r and simultaneously reduces $|\omega_i|$, indicating a stabilising influence and a lower global oscillation frequency at fixed (We, Bo, Γ). Consistently, the base state develops a sizeable polymeric tensile resistance $T_0 = \tau_{zz,0} - \tau_{rr,0} \simeq \tau_{zz,0}$, with $\tau_{rr,0}$ remaining comparatively small and $\tau_{zz,0}$ reaching $O(1)$ values for $De = 3$ and $O(10)$ values for $De = 5$ over an extended downstream region (figure 1*b*). Physically, this accumulated extensional stress provides

https://doi.org/10.1017/jfm.2026.11694 Published online by Cambridge University Press

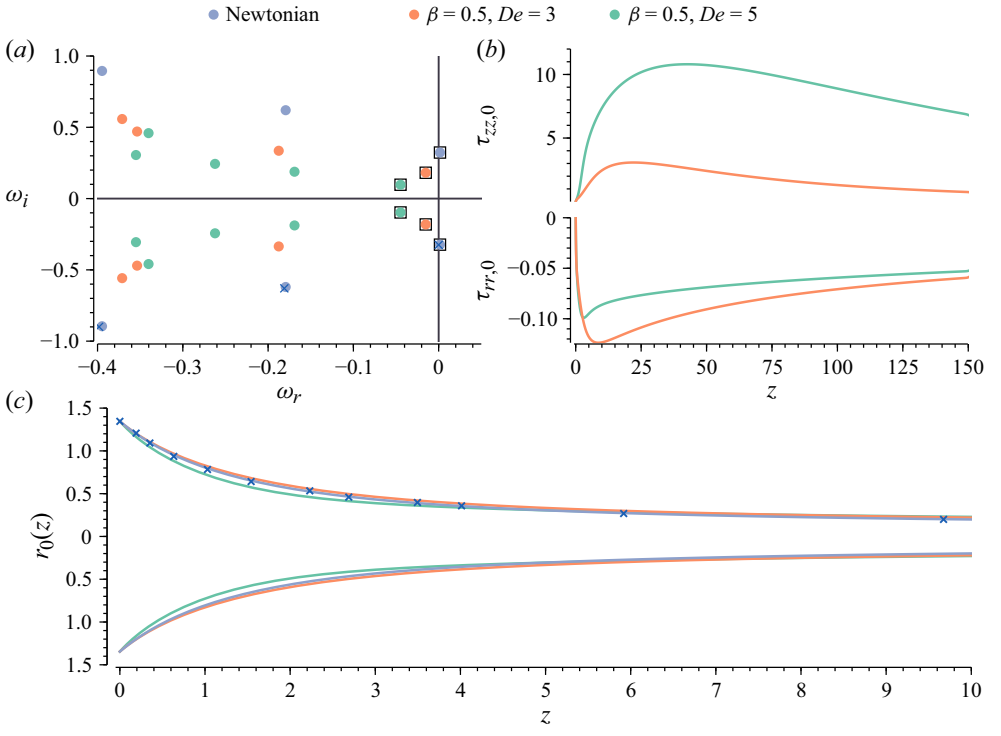


Figure 1. (*a*) Direct spectrum, where hollowed out squares mark the leading eigenvalues, (*b*) spatial evolution of the base polymeric stresses and (*c*) base jet radius, for $We = 0.003$, $Bo = 1.81$, $\Gamma = 5.83$ and selected rheology parameters (see legend). Dark blue crosses in (*a*) and (*c*) are Newtonian results from Rubio-Rubio *et al.* (2013), included for comparison.

an additional streamwise tension that competes with capillary-driven thinning, thereby lowering the global growth rate and delaying the onset of a self-excited oscillatory state (at fixed *We*). At the same time, the base radius profile remains close to the Newtonian one (figure 1*c*), with only modest quantitative changes near the nozzle. This indicates that, in the present parameter regime, viscoelasticity does not primarily act by strongly reshaping the mean jet geometry, but rather through the additional tensile-stress pathway carried by the polymer. In particular, increasing *De* does not modify the momentum coupling coefficient directly, but it slows the relaxation of the polymer stresses relative to advection and stretching, allowing $\tau_{zz,0}$ to persist farther downstream and, in the cases considered here, to reach larger magnitudes. The resulting increase in the tensile stress $T_0 = \tau_{zz,0} - \tau_{rr,0}$ then feeds back more strongly on the axial momentum balance, providing an additional resistance to capillary-driven thinning while leaving the overall jet shape only weakly altered.

4.2. *The case* $We = 7 \times 10^{-4}$, $Bo = 1.8$, $\Gamma = 5.8$, $\beta = 0.5$, $De = 5$

This case is chosen to be nearly marginal (weakly damped) in the viscoelastic regime, with a leading complex-conjugate pair $\omega \simeq -1.211 \times 10^{-6} \pm 0.08984\,\mathrm{i}$, so that the growth rate is essentially zero on the time scales of interest while a well-defined global oscillation frequency is selected. Figure 2(*a*) shows the direct spectrum, where the dominant pair lies closest to the imaginary axis and is well separated from the remaining (more strongly damped) eigenvalues, indicating that the long-time linear dynamics is governed by a

https://doi.org/10.1017/jfm.2026.11694 Published online by Cambridge University Press

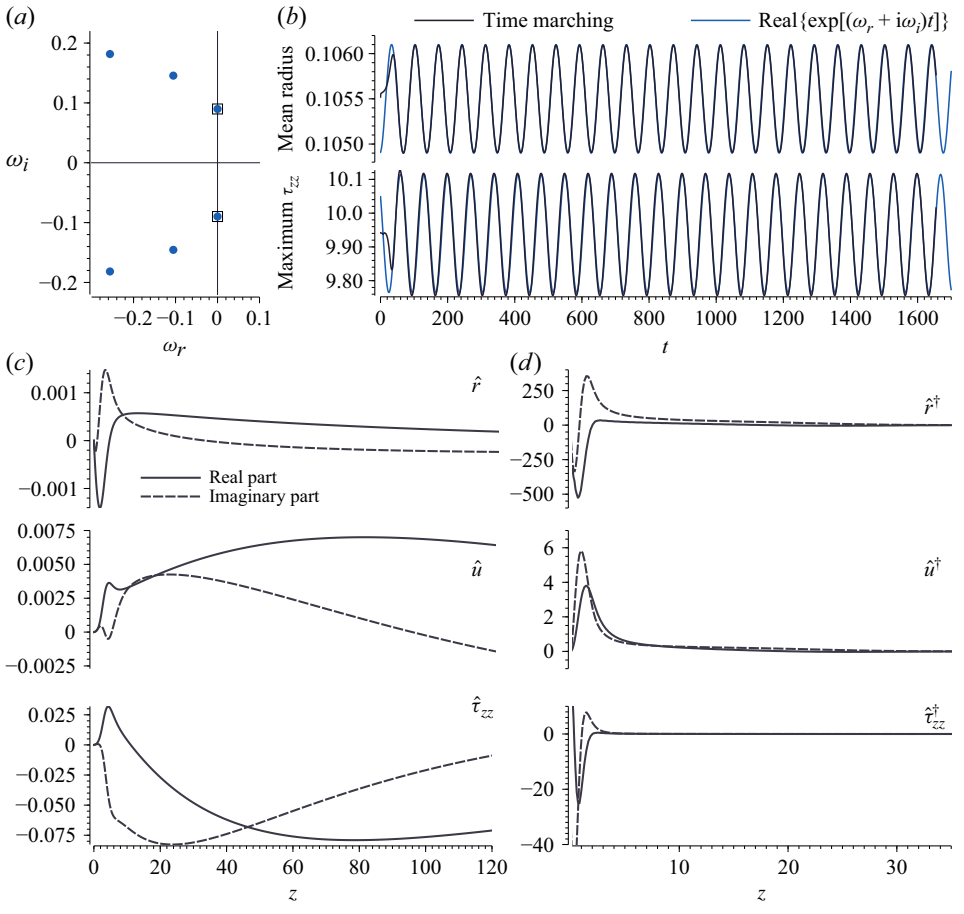


Figure 2. Marginally stable jet for $We = 7 \times 10^{-4}$, $Bo = 1.8$, $\Gamma = 5.8$, $\beta = 0.5$, $De = 5$. (*a*) Direct spectrum, for which the leading mode (marked with a square) is $\omega \simeq -1.211 \times 10^{-6} \pm 0.08984\mathrm{i}$. (*b*) Comparison between time marching and the leading linear eigenmode dynamics. (*c*) and (*d*) Direct and adjoint normalised eigenfunctions.

single global Hopf-type mode rather than by a broadband convective response, as in the Newtonian case. To validate this prediction in the fully nonlinear time-dependent equations, we perform a direct time marching of (2.9)–(2.12) using the steady base state $\boldsymbol{q}_0(z)$ as the initial condition, and we trigger the response via a small, transient inlet perturbation of the velocity

$$u(0, t) = We^{1/2} Bo^{-1/4} \left[1 + \delta\, \mathrm{e}^{-a(t-t^*)^2}\, \mathcal{H}(t - t^*)\right], \tag{4.1}$$

where $\mathcal{H}$ is the Heaviside function and $\delta = 0.01$ is sufficiently small for the ensuing evolution to remain in the linear regime and qualitatively independent of the forcing amplitude. The parameters $a = 10$ and $t^* = 10^{-3}$ control the width and onset of the notch and are selected to facilitate numerical start-up while providing a localised impulse-like excitation of the global dynamics. As shown in figure 2(*b*), both the mean radius and the maximum axial polymer stress τ_{zz} extracted from the time marching rapidly lock onto the linear prediction. After a short transient, the signals oscillate at the eigenfrequency ω_i with an envelope consistent with $\exp(\omega_r t)$ (here essentially constant owing to $|\omega_r| \ll 1$), thereby confirming the global-mode interpretation. Finally, the spatial

https://doi.org/10.1017/jfm.2026.11694 Published online by Cambridge University Press

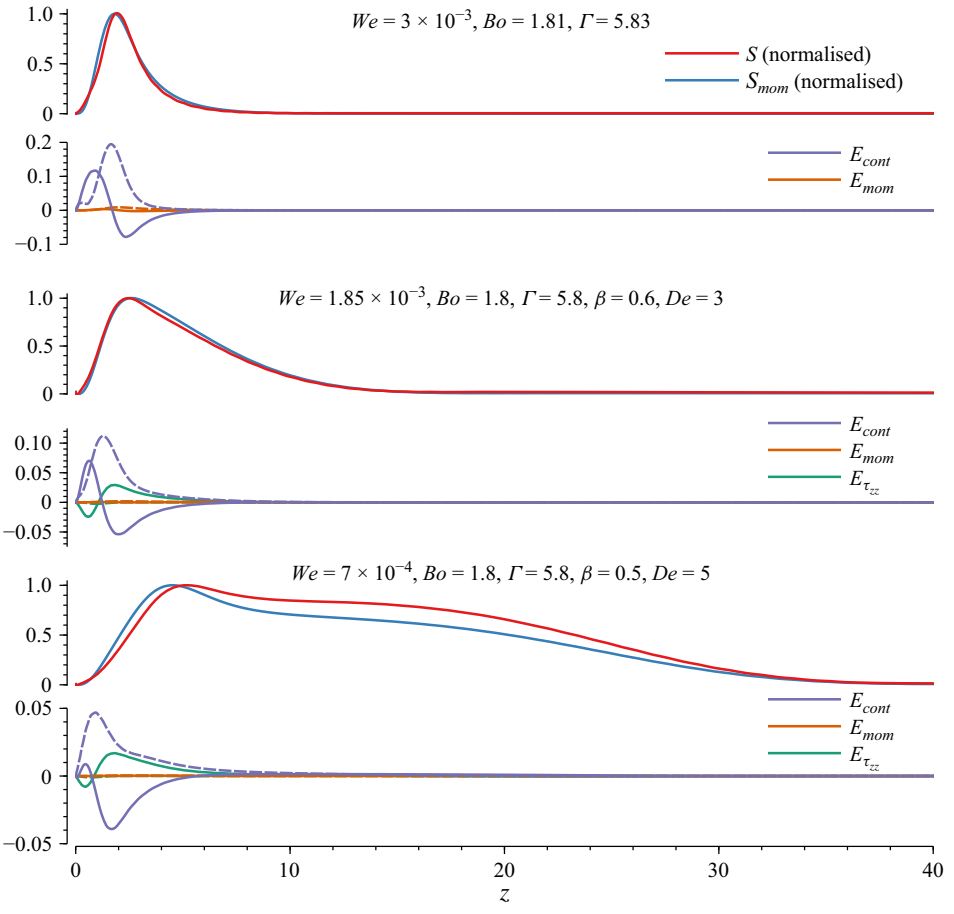


Figure 3. Wavemaker and endogeneity spatial distributions for three separate cases: $(We, Bo, \Gamma) = (3 \times 10^{-3}, 1.81, 5.83)$ (Newtonian), $(We, Bo, \Gamma, \beta, De) = (1.85 \times 10^{-3}, 1.8, 5.8, 0.6, 3)$ and $(We, Bo, \Gamma, \beta, De) = (7 \times 10^{-4}, 1.8, 5.8, 0.5, 5)$. For endogeneity computations, solid lines indicate real part, and dashed lines indicate imaginary part.

structure of the associated eigenfunctions (figure 2*c*) further supports this picture. The direct mode exhibits an extended downstream support (consistent with a convective redistribution of perturbations along the stretched jet), whereas the adjoint mode is strongly localised near the inlet, indicating that the receptivity and mode selection are controlled predominantly by the near-nozzle region. This marked upstream localisation of the adjoint fields underscores that small perturbations imposed at, or near, the inlet are the most effective at exciting the observed oscillatory response.

5. Wavemaker and endogeneity: the origin of instability

Figure 3 compares wavemaker and endogeneity diagnostics for three nearly marginal configurations, namely, a Newtonian reference case (top panels) and two viscoelastic cases of increasing elasticity (middle and bottom panels). In all three cases the parameters are chosen close to the onset of global instability, so that the leading eigenpair is weakly damped (or nearly neutral) and the associated spatial diagnostics can be interpreted as the footprint of the global feedback loop. Throughout, solid and dashed lines denote the

https://doi.org/10.1017/jfm.2026.11694 Published online by Cambridge University Press

real and imaginary parts of the endogeneity, respectively; accordingly, $\mathrm{Re}(E)$ quantifies the local contribution to the global growth/decay rate, while $\mathrm{Im}(E)$ quantifies the local contribution to the global oscillation frequency. For the Newtonian case, the normalised wavemaker $S(z)$ is sharply localised near the inlet and decays rapidly over a few nozzle radii, while $S_{mom}(z)$ is nearly indistinguishable from $S(z)$, indicating that the feedback region is compact and that restricting the structural-sensitivity tensor to the u-row captures essentially the same spatial support. Consistently, the endogeneity is dominated by the continuity/capillary pathway, i.e. E_{cont} is $O(10^{-1})$ locally and displays the expected sign structure in its real part (a positive lobe followed by a compensating negative lobe), so that the net integrated contribution remains small in the marginal limit, whereas E_{mom} is negligible in both real and imaginary parts. The imaginary component $\mathrm{Im}(E_{cont})$ is also confined to the upstream region, supporting the interpretation that the onset frequency is set primarily by the near-nozzle feedback core.

The viscoelastic cases retain the same qualitative global-oscillator signature but reveal a progressive and physically meaningful change in the spatial organisation of the sensitivity as elasticity is increased. For the intermediate case ($\beta = 0.6$, $De = 3$, middle panels), the wavemaker remains upstream peaked but its decay is already noticeably slower than in the Newtonian limit, producing a downstream tail that extends over a significantly larger fraction of the domain. This trend is further amplified in the more elastic case ($\beta = 0.5$, $De = 5$, bottom panels), for which $S(z)$ becomes markedly more distributed and remains non-negligible over an extended downstream interval. In other words, one of the most robust effects of introducing a viscoelastic dynamics in a gravitationally stretched jet is not merely a shift of the leading eigenvalue, but a pronounced spreading of the feedback-sensitive region. The instability is still selected upstream, yet the portion of the jet that participates in the global feedback loop grows with De. This behaviour is consistent with the fact that polymeric stresses are advected and relax over a finite time scale, so that elastic memory couples distant axial locations through the transport of tensile stress. At the same time, the separation between $S(z)$ and $S_{mom}(z)$ becomes increasingly apparent as elasticity grows (most clearly in the bottom case), for which $S(z)$ exceeds $S_{mom}(z)$ over much of the downstream tail, indicating that a momentum-row restriction underestimates the full structural sensitivity once viscoelastic degrees of freedom are active and confirming that the extra sensitivity is carried by the stress subspace rather than by the Newtonian momentum balance alone.

The endogeneity decomposition confirms this interpretation while highlighting that the dominant balance remains localised closer to the inlet than the wavemaker itself. In both viscoelastic cases, E_{mom} remains small, but an additional contribution associated with polymeric tension emerges through $E_{\tau_{zz}}$. This elastic contribution overlaps with the region where E_{cont} is active and provides a clear mechanism for eigenvalue selection. The onset results from a coupled capillary–elastic feedback pathway in which kinematic/capillary thinning is opposed by an additional tensile-stress response. The real parts of E_{cont} and $E_{\tau_{zz}}$ exhibit comparable magnitudes in the upstream region and partially compensate one another, which is precisely the structure expected near marginality, where the global growth rate is the small residual of competing local contributions. Meanwhile, the imaginary parts (dashed curves) remain comparatively confined to the upstream region for all three cases, indicating that the oscillation frequency is still set predominantly by the near-inlet feedback core even though viscoelasticity distributes the sensitivity farther downstream. Taken together, figure 3 supports two conclusions. First, all three configurations behave as genuine global oscillators, i.e. both wavemaker and endogeneity decay well before the outlet, indicating that the selected mode is not an artefact of domain truncation. Second, viscoelasticity modifies the instability mechanism in a specific and

https://doi.org/10.1017/jfm.2026.11694 Published online by Cambridge University Press

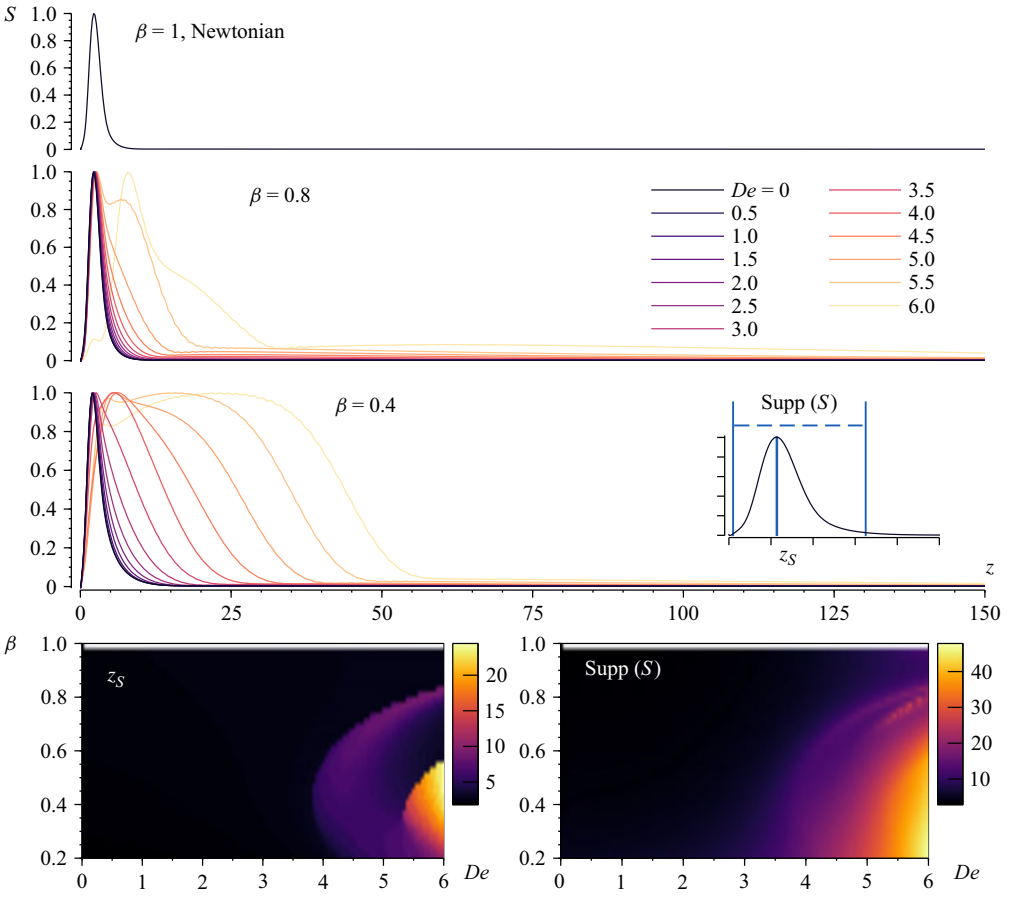


Figure 4. Spatial metrics of the wavemaker over the (β, De) parametric plane for (We, Bo, Γ) = (7×10^{-4}, 1.8, 5.8).

important way: as De increases, the feedback-sensitive region becomes progressively more widespread while a distinct polymeric endogeneity contribution appears, showing that the marginal state is controlled by a spatially distributed capillary–elastic feedback loop rather than by a purely Newtonian, near-nozzle mechanism.

To support these claims, figure 4 quantifies the redistribution of the wavemaker with elasticity using both the full profiles $S(z)$ and the scalar metrics

$$z_S = \arg\max_z S(z), \qquad \mathrm{supp}(S) = \int_0^L \frac{S(z)}{\max_z S(z)}\,\mathrm{d}z, \tag{5.1}$$

for fixed (We, Bo, Γ) = (7×10^{-4}, 1.8, 5.8) across the (β, De) parametric plane (which do not necessarily correspond to marginal cases). The Newtonian reference case exhibits a sharply localised wavemaker confined to the immediate near-nozzle region. When viscoelasticity is introduced, the dominant effect is not an abrupt displacement of the peak away from the inlet, but a progressive broadening of the downstream tail of $S(z)$ as De increases, which is already visible for $\beta = 0.8$ and becomes much more pronounced for $\beta = 0.4$. The heat maps confirm this trend quantitatively: the support length grows strongly as elasticity is increased, i.e. as De increases and β decreases, whereas the peak location z_S is comparatively less sensitive and shifts appreciably downstream only in the

https://doi.org/10.1017/jfm.2026.11694 Published online by Cambridge University Press

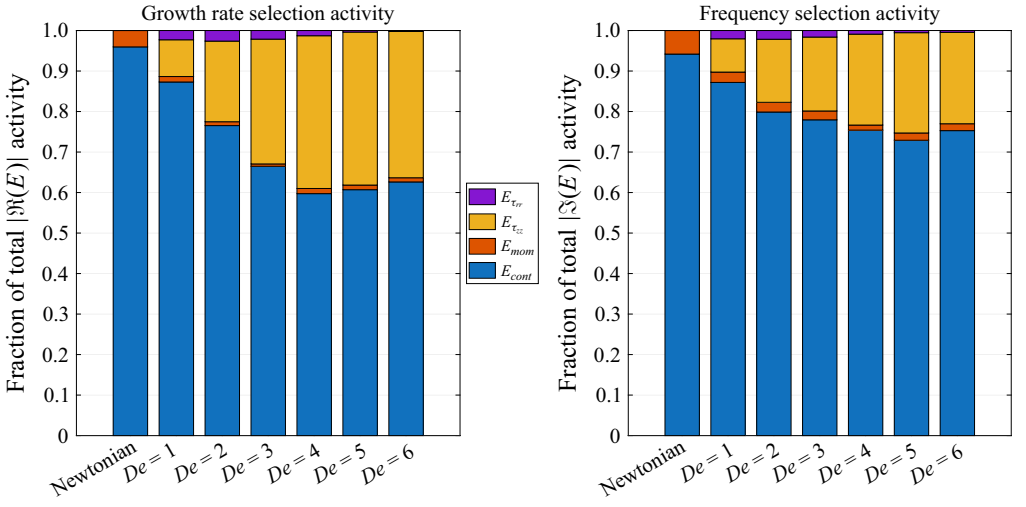


Figure 5. Endogeneity budget for $(We, Bo, \Gamma, \beta) = (7 \times 10^{-4}, 1.8, 5.8, 0.5)$ and increasing De. The Newtonian case $\beta = 1$ is included as a baseline reference.

most elastic cases. Thus, viscoelasticity does not primarily relocate the instability core; rather, it preserves an upstream-selected feedback region while enlarging the axial portion of the jet over which tensile-stress memory participates in the global feedback loop. This provides a quantitative confirmation for the interpretation drawn from the wavemaker plots alone, namely that the main viscoelastic effect is a broadening of the feedback-sensitive region rather than a simple translation of its maximum.

Additionally, figure 5 quantifies this trend by reporting the fraction of total endogeneity activity carried by each equation, using the absolute budgets of $\mathrm{Re}(E)$ and $\mathrm{Im}(E)$ so as to measure the contribution of each equation into the endogeneity budget/eigenvalue production. In the Newtonian limit, both growth-rate and frequency selections are overwhelmingly dominated by E_{cont}, with only a minor contribution from E_{mom}. As De increases, however, a distinct axial polymer-stress pathway emerges through $E_{\tau_{zz}}$. Its relative weight grows systematically, especially in the growth-rate budget, while $E_{\tau_{rr}}$ and E_{mom} remain comparatively small. Thus the viscoelastic modification of the instability is not a generic stress effect, but is carried primarily by the axial tensile response. At the same time, the continuity contribution remains dominant in the frequency budget, indicating that elasticity alters growth-rate selection more strongly than frequency selection.

6. Influence of rheology on marginal conditions

Figure 6 generalises the marginal-curve analysis by varying the viscous level over three representative Kapitza numbers, $\Gamma = 0.84$, 5.83 and 18.5, while keeping the viscosity ratio fixed at $\beta = 0.8$ and sweeping De. Each row reports the critical Weber number $We_c(Bo)$ at the onset of the self-excited global oscillation and the corresponding critical frequency $\omega_{i,c}(Bo)$. For all three values of Γ, the Newtonian reference curve decreases monotonically with Bo in both panels. Increasing the nozzle size, and therefore strengthening gravity relative to surface tension, shifts the transition to progressively smaller flow rates and to lower oscillation frequencies. This indicates that the global feedback loop becomes slower as the jet is more strongly stretched downstream. The middle row, $\Gamma = 5.83$, includes the Newtonian data of Rubio-Rubio *et al.* (2013) and recovers both the marginal branch and

https://doi.org/10.1017/jfm.2026.11694 Published online by Cambridge University Press

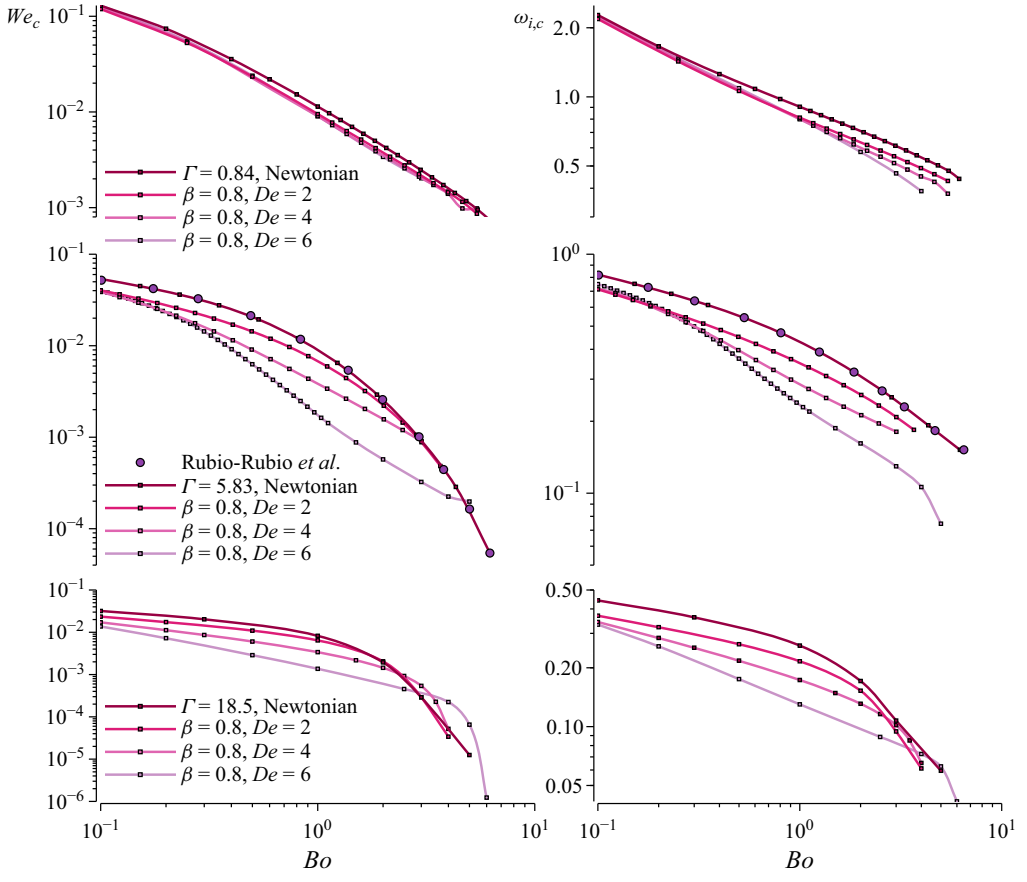


Figure 6. Marginal curves $We_c(Bo)$ and corresponding frequencies $\omega_{i,c}(Bo)$ for $\Gamma = 0.84$, 5.83 and 18.5. Dots represent individually computed marginal cases, joined by interpolating splines.

the onset frequency quantitatively, thereby extending the Newtonian benchmark of § 4.1 to the full marginal curve.

Superimposed on this Newtonian baseline, viscoelasticity produces a systematic ordering with De across the whole (Bo, Γ) range considered. For fixed (Bo, Γ), increasing De shifts both We_c and $\omega_{i,c}$ downward, so that $We_c(De = 2) > We_c(De = 4) > We_c(De = 6)$ and $\omega_{i,c}(De = 2) > \omega_{i,c}(De = 4) > \omega_{i,c}(De = 6)$, with the viscoelastic curves lying below the Newtonian one. In the present formulation this trend is interpreted in terms of an additional tensile-stress pathway. As De increases at fixed β, polymeric stresses are transported over longer axial distances before relaxing. This strengthens the base-state tensile resistance and enhances the linear coupling by which stress perturbations feed back on the free surface through the axial-tension term. In effect, elastic tension competes with capillary-driven thinning and delays the onset of the global oscillatory instability, so that marginality is reached only when the through flow is reduced, meaning smaller We. The reduction in $\omega_{i,c}$ with De is consistent with the same picture. Marginality occurs at weaker advection and the polymer introduces a memory time scale that adds phase lag to the global loop. Both effects promote slower oscillations at onset. This interpretation is consistent with the wavemaker and endogeneity diagnostics of § 5, which

https://doi.org/10.1017/jfm.2026.11694 Published online by Cambridge University Press

show that elasticity broadens the feedback-sensitive region and introduces a non-negligible polymeric contribution to eigenvalue production in marginal configurations.

Varying Γ modulates these trends in a physically informative way. Increasing Γ shifts the overall Newtonian boundary downward in We_c and in $\omega_{i,c}$, which reflects the stabilising role of viscous stresses in suppressing capillary-driven unsteadiness and permitting sustained jetting at lower flow rates. The incremental viscoelastic shift is noticeably weaker for the lowest viscous level, $\Gamma = 0.84$, where the curves nearly collapse and the dependence on De becomes mild. This near collapse is consistent with a regime in which onset is controlled by a rapid inertio-capillary balance localised near the inlet, leaving limited opportunity for polymeric stresses to accumulate and influence the marginal condition. It is also the regime where Rubio-Rubio *et al.* (2013) emphasise that additional upstream physics can become important for low-viscosity liquids issued through long injectors, in particular viscous relaxation of the exit velocity profile (see also Sevilla (2011)). By way of contrast, for $\Gamma = 5.83$ and 18.5 the viscoelastic shift is clearly resolved, especially at small-to-moderate Bo, and it weakens as Bo increases. This is consistent with the increasing dominance of gravity-driven stretching and advection at large Bo, which drives the marginal curves back towards the Newtonian scaling. Overall, figure 6 shows that moderate elasticity, $De = O(1)$, induces systematic shifts of both the critical flow rate and the onset frequency, and that these shifts depend on viscosity in a manner consistent with a coupled capillary–elastic feedback loop whose influence is strongest when the jet is not too strongly gravity dominated.

7. Conclusions

We have analysed the global stability of a one-dimensional full-curvature model for gravitationally stretched viscoelastic jets and used direct–adjoint diagnostics to interpret the instability mechanism. The framework retains the spatial development of the base state and admits a global eigenvalue formulation. This allows us to predict the onset of the jetting–dripping transition for weakly elastic liquids, and to interpret the instability mechanism using direct–adjoint diagnostics that quantify receptivity, structural sensitivity and endogeneity.

In the Newtonian limit we reproduced the benchmark results of Rubio-Rubio *et al.* (2013), including marginal spectra, base-state profiles and the dependence of the critical flow rate and onset frequency on the Bond and Kapitza numbers. This validation supports the accuracy of the numerical implementation and confirms that the onset is a genuine global instability selected by the inlet and the non-parallel base flow rather than a truncation artefact. Extending this baseline to viscoelastic liquids, we identified robust shifts of the leading Hopf eigenpair as elasticity is increased. For fixed (Bo, Γ) and viscosity ratio β, increasing the Deborah number decreases both the critical Weber number and the selected onset frequency. This trend persists across the three viscous levels considered, and it is most pronounced at small-to-moderate Bo while weakening as Bo increases and gravity-driven stretching becomes dominant.

The direct–adjoint diagnostics provide a mechanistic interpretation of these parametric trends. In Newtonian jets the wavemaker is sharply localised near the inlet and the endogeneity is dominated by the continuity and capillarity pathway, with momentum contributions remaining comparatively small in marginal configurations. When viscoelasticity is introduced, the instability retains its upstream-selected global-oscillator character, but the feedback-sensitive region spreads downstream in a systematic way as De increases. This spreading reflects the advection and relaxation of polymeric

https://doi.org/10.1017/jfm.2026.11694 Published online by Cambridge University Press

stresses, and it is accompanied by a distinct polymeric contribution to eigenvalue production. Physically, this means that elasticity does not relocate the instability core away from the nozzle, but enlarges the axial segment over which tensile-stress memory participates in the global feedback loop. In marginal cases, the real parts of the continuity-driven and stress-driven endogeneities partially compensate, which indicates that onset is governed by a coupled capillary–elastic feedback loop rather than by a purely Newtonian balance. The imaginary components remain concentrated closer to the inlet, which supports the view that the oscillation frequency is set predominantly by the near-nozzle core even when viscoelasticity distributes sensitivity farther downstream.

Although a direct quantitative experimental validation of the present marginal curves is not available here, the predicted trends are qualitatively consistent with observations in related viscoelastic jetting configurations. In particular, Clasen *et al.* (2009) report that dilute polymer solutions sustain jetting at substantially smaller critical flow rates than water, and that near transition the dynamics becomes more spatially extended and strongly dependent on the breakup kinetics of viscoelastic ligaments. Those experiments, although well beyond the onset of criticality, also show that the transition is sensitive to polymer concentration, solution freshness and nozzle-exit conditions, which is broadly compatible with the strong inlet receptivity identified by the present direct–adjoint analysis.

Several extensions follow naturally. First, the influence of more elaborate inlet-stress closures could be assessed systematically with the same receptivity tools used here. Second, the present framework is well suited to resolvent and forced-response analyses, which would help connect global stability with noise amplification and the intermittency observed near marginality. Third, additional physics such as viscous relaxation of the exit velocity profile, weak confinement or surface-active effects should be incorporated in order to allow a more direct comparison with experiments in low-viscosity regimes and to clarify the interplay between axial-curvature stabilisation and viscoelastic tension. In particular, the recent experiments and global analysis of Sun *et al.* (2026) show that velocity relaxation at the nozzle exit can lower the critical Weber number by generating a strongly non-parallel disturbance field in the upstream relaxation region, a mechanism that lies outside reduced free-jet descriptions such as the present one. Extending the model to include nozzle-exit relaxation physics is therefore a natural next step, especially for low-viscosity liquids and long injectors, where threshold selection may depend on both the upstream relaxation and downstream capillary–elastic dynamics. More broadly, the results suggest that one of the main effects of weak elasticity in stretched jets is not just an eigenvalue drift, but a redistribution of the feedback-sensitive region along the jet, with direct implications for modelling, reduced-order descriptions and control strategies for jetting and dispensing processes.

Acknowledgements. Professors M. Rubio-Rubio and A. Sevilla are thanked for fruitful discussions. Generative artificial intelligence tools have been used for: (i) code debugging, (ii) helping in writing sections § 1 and § 6 and (iii) identification of related bibliography.

Funding. This work has been supported by the Spanish MINECO under project PID2020-115655GB-C22, partly financed through FEDER European funds.

Declaration of interests. The author reports no conflict of interest.

Appendix A. Explicit linearised equations

We linearise the dimensionless governing (2.9)–(2.12) about a steady base state $\boldsymbol{q}_0(z) = [r_0, u_0, \tau_{zz,0}, \tau_{rr,0}]^{\mathrm{T}}$ and seek normal modes $\hat{\boldsymbol{q}}(z) = [\hat{r}, \hat{u}, \hat{\tau}_{zz}, \hat{\tau}_{rr}]^T$ such that $\boldsymbol{q}(z, t) = \boldsymbol{q}_0(z) + \epsilon\, \hat{\boldsymbol{q}}(z)\mathrm{e}^{\omega t}$, with $\epsilon \ll 1$. Throughout, primes denote derivatives with respect

https://doi.org/10.1017/jfm.2026.11694 Published online by Cambridge University Press

to z. When the perturbation enters through a nonlinear functional of the base state (e.g. curvature or conservative fluxes), we employ the first variation (Fréchet derivative) notation

$$\delta F \equiv \frac{\mathrm{d}}{\mathrm{d}\epsilon}\, F\big[r_0+\epsilon\hat{r},\ u_0+\epsilon\hat{u},\ \tau_{zz,0}+\epsilon\hat{\tau}_{zz},\ \tau_{rr,0}+\epsilon\hat{\tau}_{rr}\big]\Big|_{\epsilon=0}. \tag{A1}$$

With this convention, the linearised system can be written compactly as $(\boldsymbol{A}-\omega\boldsymbol{B})\hat{\boldsymbol{q}}=\boldsymbol{0}$, where $\boldsymbol{B}$ collects the temporal (mass-matrix) terms and $\boldsymbol{A}$ collects spatial derivatives and couplings. Thus, the linearised mass conservation and momentum laws read

$$\omega\,(2r_0\hat{r})+\partial_z\Big(2r_0u_0\hat{r}+r_0^2\hat{u}\Big)=0, \tag{A2}$$

$$\omega\hat{u}+u_0\hat{u}'+u_0'\hat{u}=-\partial_z(\delta C)+\Gamma\,\delta\bigg[\frac{1}{r^2}\partial_z\Big(r^2u'\Big)\bigg] + \frac{\Gamma(1-\beta)}{3\beta}\,\delta\bigg[\frac{1}{r^2}\partial_z\Big(r^2T\Big)\bigg], \tag{A3}$$

where $T=\tau_{zz}-\tau_{rr}$ and δC is the first variation of the full curvature (2.3). The explicit expression for δC follows by differentiating the curvature functional (2.3). Introducing $s_0=(1+r_0'^2)^{-1/2}$, we obtain

$$\delta C=-\frac{s_0}{r_0^2}\hat{r}-\frac{r_0's_0^3}{r_0}\hat{r}'-s_0^3\hat{r}''+3\,r_0''\,r_0'\,s_0^5\,\hat{r}'. \tag{A4}$$

For implementation purposes, it is also useful to expand the conservative flux variations appearing in (A3). Denoting $\hat{T}=\hat{\tau}_{zz}-\hat{\tau}_{rr}$, one convenient form is

$$\delta\bigg[\frac{1}{r^2}\partial_z\Big(r^2u'\Big)\bigg]=-\frac{2\hat{r}}{r_0^3}\partial_z\Big(r_0^2u_0'\Big)+\frac{1}{r_0^2}\partial_z\Big(2r_0\hat{r}\,u_0'+r_0^2\hat{u}'\Big), \tag{A5}$$

$$\delta\bigg[\frac{1}{r^2}\partial_z\Big(r^2T\Big)\bigg]=-\frac{2\hat{r}}{r_0^3}\partial_z\Big(r_0^2T_0\Big)+\frac{1}{r_0^2}\partial_z\Big(2r_0\hat{r}\,T_0+r_0^2\hat{T}\Big), \tag{A6}$$

with $T_0=\tau_{zz,0}-\tau_{rr,0}$. Finally, the diagonal Giesekus constitutive laws (2.5)–(2.6) linearise to

$$De\big(\omega\hat{\tau}_{zz}+u_0\hat{\tau}_{zz}'+\hat{u}\,\tau_{zz,0}'-2u_0'\hat{\tau}_{zz}-2\hat{u}'\tau_{zz,0}\big)+\hat{\tau}_{zz}+2\alpha De\,\tau_{zz,0}\hat{\tau}_{zz}=2\hat{u}', \tag{A7}$$

$$De\big(\omega\hat{\tau}_{rr}+u_0\hat{\tau}_{rr}'+\hat{u}\,\tau_{rr,0}'+u_0'\hat{\tau}_{rr}+\hat{u}'\tau_{rr,0}\big)+\hat{\tau}_{rr}+2\alpha De\,\tau_{rr,0}\hat{\tau}_{rr}=-\hat{u}'. \tag{A8}$$

In the Newtonian limit $De=0$ (or $1-\beta=0$ in the momentum coupling), these constitutive equations are dropped and the tensile-stress contribution in (A3) vanishes.

The eigenmode boundary conditions follow from the fact that inlet data are prescribed; thus, perturbations satisfy homogeneous inlet conditions

$$\hat{r}(0)=0,\qquad \hat{u}(0)=0,\qquad \hat{\tau}_{zz}(0)=0,\qquad \hat{\tau}_{rr}(0)=0, \tag{A9}$$

whereas at the downstream boundary $z=L$, we impose homogeneous outflow conditions

$$\hat{r}'(L)=0,\quad \hat{r}''(L)=0,\quad \hat{u}'(L)=0. \tag{A10}$$

For sufficiently large L, the leading eigenvalues are insensitive to the specific admissible outflow choice provided the instability core remains well upstream of the truncation.

https://doi.org/10.1017/jfm.2026.11694 Published online by Cambridge University Press

Appendix B. Numerical methodology and sensitivity

To solve both the base flow, obtained by setting temporal derivatives of (2.9)–(2.12) to zero and eliminating the velocity from continuity, i.e. $r_0^2 u_0 = Bo^{3/4} We^{1/2}$, and the generalised eigenvalue problem (3.2), we discretised the corresponding differential operators using a standard Chebyshev collocation method (Trefethen 2000). The physical domain $0 \leqslant z \leqslant L$ is mapped onto a Gauss–Lobatto grid $\xi_j = \cos[\pi(j-1)/(N-1)]$, $j = 1, \ldots, N$, with $-1 \leqslant \xi \leqslant 1$ and N the number of grid points. In the calculations reported here the mapping $z(\xi)$ was taken to be linear, and no additional clustering of the collocation points was found to be necessary. Derivatives with respect to ξ are computed by the standard Chebyshev differentiation matrices and then transformed to the physical coordinate z through the chain rule. In particular, the derivative of the full curvature appearing in the momentum equation is represented directly in collocation form by combining first-, second- and third-order differentiation matrices with the appropriate variable coefficients, so that the third-order axial structure associated with $\partial_z \mathcal{C}$ is retained explicitly at the discrete level. The nonlinear boundary-value problem for the base flow is solved by a damped Newton–Raphson iteration with relaxation and backtracking. Boundary conditions are enforced algebraically by row replacement in the assembled residual and Jacobian matrices: for the base state we impose $r_0(0) = Bo^{1/2}$, $\tau_{zz,0}(0) = \tau_{rr,0}(0) = 0$, together with the straight-jet conditions $r_0'(L) = r_0''(L) = 0$. Once the base state is obtained, the linearised problem is assembled in matrix-pencil form $(\boldsymbol{A} - \omega \boldsymbol{B})\tilde{\boldsymbol{q}} = 0$, and the leading eigenvalues are extracted with the standard MATLAB routine `eigs` in shift-and-invert mode. For the perturbation problem, the homogeneous inlet conditions are imposed by the same row-replacement procedure.

The adjoint modes used throughout this paper are obtained as the strict discrete adjoint of the assembled matrix pencil, rather than from a separately derived continuous adjoint followed by discretisation. More precisely, after solving the direct problem for the right eigenvectors of $(\boldsymbol{A}, \boldsymbol{B})$, we solve the corresponding left eigenvalue problem associated with $\boldsymbol{A}^{\mathrm{H}}$ and $\boldsymbol{B}^{\mathrm{H}}$ and then convert the resulting Euclidean left eigenvectors into Q-adjoint modes through the quadrature-weighted inner product introduced in (3.3). In practice, the scalar quadrature weights are computed from Clenshaw–Curtis quadrature (Trefethen 2000) on $[0, L]$ and assembled into a diagonal matrix $\boldsymbol{Q}_z$, which is then extended to the full state vector as $\boldsymbol{Q} = \mathrm{blkdiag}(\boldsymbol{Q}_z, \boldsymbol{Q}_z, \boldsymbol{Q}_z, \boldsymbol{Q}_z)$. Direct modes are first normalised to unit Q-norm, $\langle \tilde{\boldsymbol{q}}, \tilde{\boldsymbol{q}} \rangle_Q = 1$, and the adjoint modes are subsequently rescaled so as to satisfy the bi-orthogonality condition $\langle \tilde{\boldsymbol{q}}^{\dagger}, \boldsymbol{B}\tilde{\boldsymbol{q}} \rangle_Q = 1$.

Although the results reported in the present paper were computed with values of L and N in the ranges $120 \leqslant L \leqslant 300$ and $64 \leqslant N \leqslant 256$, respectively, depending on the parameter set and figure family, we have carefully verified that both the base flow and the leading eigenvalue are insensitive to further increases in these numerical parameters. To document this, we perform two complementary audits. First, at fixed L we vary N and monitor the leading eigenvalue $\omega = \omega_r + \mathrm{i}\omega_i$, together with the peak polymeric tensile stress $T_{0,max}$ and its axial location $z_{T_{0,max}}$. In addition, we report the base-state jet radius and velocity at a fixed representative downstream location, namely $r_0(20)$ and $u_0(20)$. Second, at fixed N we vary the truncation length L and track the same quantities in order to verify that both the base flow and the leading eigenvalue have converged with respect to domain length. The corresponding results are presented below in table 1 for the nearly marginal case $Bo = 1$, $We = 0.01$, $\Gamma = 5.83$, $\beta = 0.8$, $De = 1$. These tables show that the reported leading eigenpair is already converged to the digits quoted in the manuscript and that the base-state quantities entering the viscoelastic-stress and wavemaker diagnostics are likewise insensitive to further refinement.

https://doi.org/10.1017/jfm.2026.11694 Published online by Cambridge University Press

N	L	ω_r	ω_i	$T_{0,max}$	$z_{T_{0,max}}$	$r_0(20)$	$u_0(20)$
64	200	−0.007 996	0.395 460	1.102 000	9.903 113	0.152 644	4.291 743
96	200	−0.008 463	0.395 070	1.103 185	9.099 346	0.152 600	4.294 301
128	200	−0.008 460	0.395 066	1.103 712	8.712 655	0.152 601	4.294 244
160	200	−0.008 460	0.395 066	1.103 470	8.485 438	0.152 601	4.294 254
192	200	−0.008 460	0.395 066	1.103 195	9.005 768	0.152 601	4.294 254
256	200	−0.008 460	0.395 066	1.103 687	8.645 454	0.152 601	4.294 254
N	L	ω_r	ω_i	$T_{0,max}$	$z_{T_{0,max}}$	$r_0(20)$	$u_0(20)$
160	120	−0.008 460	0.395 066	1.103 355	8.950 295	0.152 601	4.294 254
160	160	−0.008 460	0.395 066	1.103 602	8.827 433	0.152 601	4.294 254
160	200	−0.008 460	0.395 066	1.103 470	8.485 438	0.152 601	4.294 254
160	240	−0.008 460	0.395 066	1.103 091	8.357 135	0.152 600	4.294 254
160	300	−0.008 460	0.395 066	1.103 193	8.382 576	0.152 601	4.294 250

Table 1. Numerical audit for the nearly marginal case $Bo = 1$, $We = 0.01$, $\Gamma = 5.83$, $\beta = 0.8$, $De = 1$.

Appendix C. The influence of polymer-stress inlet boundary conditions

The inlet treatment of the polymer stresses is one of the main modelling assumptions of the present reduced free-jet formulation. In the body of the paper we adopt the fully relaxed condition

$$\tau_{zz}(0, t) = \tau_{rr}(0, t) = 0, \tag{C1}$$

as a baseline closure. This is appropriate when the fluid exits the nozzle with little elastic memory, but it is not expected to be universally accurate in experiments, where die swell and upstream rheology may generate non-zero stresses at the exit (Clasen *et al.* 2009; Mitsoulis 2010). The purpose of this appendix is therefore simply to assess whether the main global-stability conclusions are materially affected by moderate non-zero inlet stresses.

To that end, we considered two alternative closures. The first is a Taylor-series motivated relation, in the spirit of Alhushaybari & Uddin (2019), obtained by evaluating the steady constitutive equations at the nozzle and replacing the inlet stresses by their Newtonian-equivalent values. The second is a broader ad hoc family of finite inlet stresses that allows the total inlet tension and its partition between axial and radial components to be varied systematically.

C.1. *Taylor-series motivated closure*

Consider the steady one-dimensional system together with the inlet conditions

$$r_0(0) = Bo^{1/2}, \qquad u_0(0) = We^{1/2}Bo^{-1/4}. \tag{C2}$$

Expanding the steady fields for $z \to 0^+$ and collecting leading-order terms shows that the inlet values of $\tau_{zz,0}(0)$ and $\tau_{rr,0}(0)$ are not uniquely fixed by the outer free-jet equations alone, because their nozzle derivatives also enter. Thus, as in related slender analyses (Alhushaybari & Uddin 2019), an additional closure assumption is still required. Following that approach, we replace the inlet stresses by their Newtonian-equivalent values, i.e. we set $De = 0$ in the constitutive equations at the nozzle. In the present scaling this yields

$$\tau_{zz,0}(0) = 2u_0'(0), \qquad \tau_{rr,0}(0) = -u_0'(0), \tag{C3}$$

https://doi.org/10.1017/jfm.2026.11694 Published online by Cambridge University Press

or equivalently

$$T_0(0) = \tau_{zz,0}(0) - \tau_{rr,0}(0) = 3u_0'(0). \tag{C4}$$

This should be interpreted as an asymptotically motivated effective inlet closure, not as a resolved nozzle-to-jet matching law. For the linearised eigenproblem, the inlet data remain prescribed at the base-state level, and the corresponding perturbation conditions are homogeneous

$$\hat{r}(0) = \hat{u}(0) = \hat{\tau}_{zz}(0) - 2\hat{u}'(0) = \hat{\tau}_{rr}(0) + \hat{u}'(0) = 0. \tag{C5}$$

Relative to the baseline relaxed case $\tau_{zz}(0) = \tau_{rr}(0) = 0$, the leading eigenvalue changed only from $\omega = -0.0021 + 0.0892\,\mathrm{i}$ to $\omega = -0.0019 + 0.0904\,\mathrm{i}$, i.e. a very small absolute shift in both growth rate and frequency, while the corresponding eigenfunctions remained almost unchanged except within a very thin region adjacent to the nozzle.

C.2. *A two-parameter ad hoc inlet-stress family*

To probe the sensitivity of the global spectrum more broadly, we also consider the family

$$\tau_{zz,0}(0) = \chi\ \tau^*, \qquad \tau_{rr,0}(0) = -(1-\chi)\ \tau^*, \tag{C6}$$

where τ^* sets the magnitude of the imposed inlet stress and χ controls its partition between axial and radial components. This simple parameterisation preserves a one-parameter control of the inlet tensile stress

$$T_0(0) = \tau_{zz,0}(0) - \tau_{rr,0}(0) = \tau^*, \tag{C7}$$

while allowing the individual diagonal stresses to vary over a broad range. In particular, $\chi = 1$ or $\chi = 0$ produce purely axial or purely radial realisations of the same net inlet tension. For the eigenproblem associated with (C6), the perturbation inlet conditions are again homogeneous.

C.3. *Numerical protocol*

The sensitivity tests were carried out for the representative nearly marginal viscoelastic case

$$\Gamma = 5.8, \qquad \beta = 0.5, \qquad De = 5, \qquad Bo = 1.8, \qquad We = 7 \times 10^{-4}, \tag{C8}$$

with computational length $L = 180$. For each inlet closure, the steady base state was recomputed by Newton iteration using the modified inlet values of $\tau_{zz,0}(0)$ and $\tau_{rr,0}(0)$. The generalised eigenvalue problem was then reassembled and solved using the same Chebyshev discretisation and adjoint normalisation described in § 3. The leading mode was identified as the eigenpair with largest temporal growth rate $\mathrm{Re}(\omega)$. To assess whether the mechanistic interpretation changed, we compared not only the leading eigenvalue but also the real parts of the stress components of the direct mode and the normalised full wavemaker.

Results are presented in figure 7. For the global spectra, the shift in the leading eigenvalue is marginal, and the whole spectrum remains essentially unchanged across the full range $0 \leqslant \chi \leqslant 1.2$. In particular, the dominant complex-conjugate pair exhibits only a very small drift in the inset, while the damped branches are practically superposed. Thus, redistributing the imposed inlet stress between axial and radial components does not materially alter the selected global Hopf mode. The base polymer stresses are affected mainly within a short entrance region. As shown in figure 7(*b*), the imposed values of $\tau_{zz,0}(0)$ and $\tau_{rr,0}(0)$ vary with χ as prescribed, but these differences relax rapidly

https://doi.org/10.1017/jfm.2026.11694 Published online by Cambridge University Press

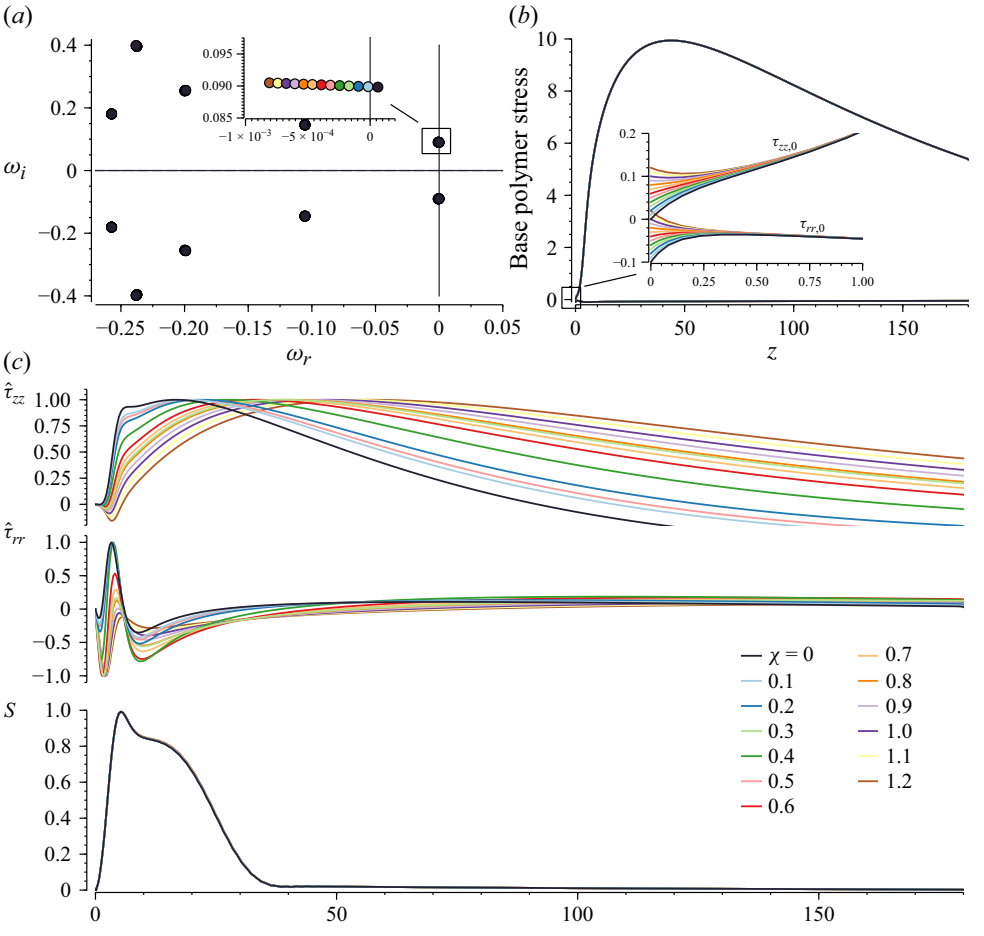


Figure 7. Variation of (*a*) global spectra, (*b*) base-flow polymer stresses and (*c*) direct polymer-stress eigenfunctions, and wavemaker with χ.

downstream, so that the base tensile-stress profiles nearly collapse beyond the inlet layer. The real parts of the direct stress eigenfunctions show the same behaviour: $\hat{\tau}_{zz}$ retains the same broad positive lobe and downstream decay for all χ, with only mild differences in the far tail, while $\hat{\tau}_{rr}$ is even less sensitive and rapidly collapses after the near-nozzle oscillatory structure. Most importantly, the normalised wavemaker distributions are nearly indistinguishable for all values of χ. The peak remains located in the same compact upstream region and the sensitivity decays over essentially the same axial interval in every case. Hence, for the representative near-critical viscoelastic case (C8), the leading eigenpair, the downstream base state and the feedback-sensitive region are all remarkably insensitive to moderate $O(10^{-1})$ non-zero inlet stresses. This supports the view that the main mechanistic conclusions of the paper are controlled primarily by the downstream stretched-jet dynamics rather than by the precise form of the effective inlet-stress closure.

References

ALHUSHAYBARI, A. & UDDIN, J. 2019 Convective and absolute instability of viscoelastic liquid jets in the presence of gravity. *Phys. Fluids* **31** (4), 044106.

AMBRAVANESWARAN, B., SUBRAMANI, H.J., PHILLIPS, S.D. & BASARAN, O.A. 2004 Dripping-jetting transitions in a dripping faucet. *Phys. Rev. Lett.* **93** (3), 034501.

https://doi.org/10.1017/jfm.2026.11694 Published online by Cambridge University Press

ANNA, S.L., BONTOUX, N. & STONE, H.A. 2003 Formation of dispersions using 'flow focusing' in microchannels. *Appl. Phys. Lett.* **82** (3), 364–366.
ARDEKANI, A.M., SHARMA, V. & MCKINLEY, G.H. 2010 Dynamics of bead formation, filament thinning and breakup in weakly viscoelastic jets. *J. Fluid Mech.* **665**, 46–56.
BARRERO, A. & LOSCERTALES, I.G. 2007 Micro- and nanoparticles via capillary flows. *Annu. Rev. Fluid Mech.* **39** (1), 89–106.
BASARAN, O.A. 2002 Small-scale free surface flows with breakup: drop formation and emerging applications. *AICHE J.* **48** (9), 1842.
CASTRO-HERNÁNDEZ, E., CAMPO-CORTÉS, F. & GORDILLO, J.M. 2012 Slender-body theory for the generation of micrometre-sized emulsions through tip streaming. *J. Fluid Mech.* **698**, 423–445.
CLANET, C. & LASHERAS, J.C. 1999 Transition from dripping to jetting. *J. Fluid Mech.* **383**, 307–326.
CLASEN, C., BICO, J., ENTOV, V.M. & MCKINLEY, G.H. 2009 'Gobbling drops': the jetting–dripping transition in flows of polymer solutions. *J. Fluid Mech.* **636**, 5–40.
CLASEN, C., PHILLIPS, P.M., PALANGETIC, L. & VERMANT, J. 2012 Dispensing of rheologically complex fluids: the map of misery. *AICHE J.* **58** (10), 3242–3255.
DENN, M.M. 1980 Continuous drawing of liquids to form fibers. *Annu. Rev. Fluid Mech.* **12** (1), 365–387.
DOSHI, J. & RENEKER, D.H. 1995 Electrospinning process and applications of electrospun fibers. *J. Electrostat.* **35** (2–3), 151–160.
EGGERS, J. & DUPONT, T.F. 1994 Drop formation in a one-dimensional approximation of the Navier–Stokes equation. *J. Fluid Mech.* **262**, 205–221.
EGGERS, J. & VILLERMAUX, E. 2008 Physics of liquid jets. *Rep. Prog. Phys.* **71** (3), 036601.
GARCÍA, F.J. & CASTELLANOS, A. 1994 One-dimensional models for slender axisymmetric viscous liquid jets. *Phys. Fluids* **6** (8), 2676–2689.
GAÑÁN-CALVO, A.M. 1998 Generation of steady liquid microthreads and micron-sized monodisperse sprays in gas streams. *Phys. Rev. Lett.* **80** (2), 285.
GAÑÁN-CALVO, A.M. & GORDILLO, J.M. 2001 Perfectly monodisperse microbubbling by capillary flow focusing. *Phys. Rev. Lett.* **87** (27), 274501.
GIANNETTI, F. & LUCHINI, P. 2007 Structural sensitivity of the first instability of the cylinder wake. *J. Fluid Mech.* **581**, 167–197.
KELLER, J.B., RUBINOW, S.I. & TU, Y. 1973 Spatial instability of a jet. *Phys. Fluids* **16** (12), 2052–2055.
LE DIZÈS, S. 1997 Global modes in falling capillary jets. *Eur. J. Mech. B/Fluids* **16**, 761–778.
LE DIZÈS, S. & VILLERMAUX, E. 2017 Capillary jet breakup by noise amplification. *J. Fluid Mech.* **810**, 281–306.
LEIB, S.J. & GOLDSTEIN, M.E. 1986 The generation of capillary instabilities on a liquid jet. *J. Fluid Mech.* **168**, 479–500.
LOSCERTALES, I.G., BARRERO, A., GUERRERO, I., CORTIJO, R., MARQUEZ, M. & GAÑÁN-CALVO, A.M. 2002 Micro/nano encapsulation via electrified coaxial liquid jets. *Science* **295** (5560), 1695–1698.
MARQUET, O. & LESSHAFFT, L. 2015 Identifying the active flow regions that drive linear and nonlinear instabilities. arXiv preprint arXiv:1508.07620.
MARTÍNEZ-CALVO, A., RUBIO-RUBIO, M. & SEVILLA, A. 2018 The nonlinear states of viscous capillary jets confined in the axial direction. *J. Fluid Mech.* **834**, 335–358.
MARÍN, A.G., CAMPO-CORTÉS, F. & GORDILLO, J.M. 2009 Generation of micron-sized drops and bubbles through viscous coflows. *Colloid Surf. A-Physicochem. Engng Asp.* **344** (1–3), 2–7.
MARÍN, A.G., LOSCERTALES, I.G., MARQUEZ, M. & BARRERO, A. 2007 Simple and double emulsions via coaxial jet electrosprays. *Phys. Rev. Lett.* **98** (1), 014502.
MITSOULIS, E. 2010 Extrudate swell of boger fluids. *J. Non-Newtonian Fluid Mech.* **165** (13–14), 812–824.
MONTANERO, J.M. 2024 *Tip Streaming of Simple and Complex Fluids*. Springer Nature.
MONTANERO, J.M. & GAÑÁN-CALVO, A.M. 2008 Viscoelastic effects on the jetting–dripping transition in co-flowing capillary jets. *J. Fluid Mech.* **610**, 249–260.
PEARSON, J.R.A. & MATOVICH, M.A. 1969 Spinning a molten threadline. stability. *Ind. Engng Chem. Fund.* **8** (4), 605–609.
PRALITS, J.O., BRANDT, L. & GIANNETTI, F. 2010 Instability and sensitivity of the flow around a rotating circular cylinder. *J. Fluid Mech.* **650**, 513–536.
RUBIO-RUBIO, M., SEVILLA, A. & GORDILLO, J.M. 2013 On the thinnest steady threads obtained by gravitational stretching of capillary jets. *J. Fluid Mech.* **729**, 471–483.
SAUTER, U.S. & BUGGISCH, H.W. 2005 Stability of initially slow viscous jets driven by gravity. *J. Fluid Mech.* **533**, 237–257.
SCHULKES, R.M.S.M. 1994 The evolution and bifurcation of a pendant drop. *J. Fluid Mech.* **278**, 83–100.
SENCHENKO, S. & BOHR, T. 2004 The shape and stability of a viscous thread. *Phys. Rev. E* **71**, 053601.

https://doi.org/10.1017/jfm.2026.11694 Published online by Cambridge University Press

SEVILLA, A. 2011 The effect of viscous relaxation on the spatiotemporal stability of capillary jets. *J. Fluid Mech.* **684**, 204–226.

SHUKLA, I. & GALLAIRE, F. 2020 Frequency selection in a gravitationally stretched capillary jet in the jetting regime. *J. Fluid Mech.* **894**, A6.

STONE, H.A., STROOCK, A.D. & AJDARI, A. 2004 Engineering flows in small devices: microfluidics toward a lab-on-a-chip. *Annu. Rev. Fluid Mech.* **36** (1), 381–411.

SUN, H., LIU, Q., ZHANG, D., JI, B., YANG, L. & FU, Q. 2024 Global stability analysis of falling jets with surfactants. *Phys. Rev. Fluids* **9** (12), 124004.

SUN, H., ZHANG, D., LIU, Q., YANG, L., FU, Q. & JI, B. 2026 Dripping–jetting transition of a capillary jet with velocity relaxation. *J. Fluid Mech.* **1030**, A32.

SURYO, R. & BASARAN, O.A. 2006 Tip streaming from a liquid drop forming from a tube in a co-flowing outer fluid. *Phys. Fluids* **18** (8), 082102.

TREFETHEN, L.N. 2000 *Spectral Methods in MATLAB*. SIAM.

UTADA, A.S., FERNANDEZ-NIEVES, A., STONE, H.A. & WEITZ, D.A. 2007 Dripping to jetting transitions in coflowing liquid streams. *Phys. Rev. Lett.* **99** (9), 094502.

https://doi.org/10.1017/jfm.2026.11694 Published online by Cambridge University Press